Addiction-associated genetic variants implicate brain cell type- and region-specific cis-regulatory elements in addiction neurobiology

Chaitanya Srinivasan[1*], BaDoi N. Phan[1,2*], Alyssa J. Lawler[3], Easwaran Ramamurthy[1], Michael Kleyman[1], Ashley R. Brown[1], Irene M. Kaplow[1,4], Morgan E. Wirthlin[1,4], Andreas R. Pfenning [1,3,4,‡]

[1]Computational Biology Department, School of Computer Science, Carnegie Mellon University, 15213
[2]Medical Scientist Training Program, School of Medicine, University of Pittsburgh, 15213
[3]Department of Biological Sciences, Mellon College of Science, Carnegie Mellon University, 15213
[4]Neuroscience Institute, Carnegie Mellon University, 15213
[*]CS and BNP contributed equally to the work
[‡]Direct correspondence to apfenning@cmu.edu

Number of pages: **63** pages of text, 11 pages of figures

Number of figures:
- 5 main figures
- 6 supplemental figures
- **2 supplemental tables**

Number of words
- Abstract + Significance Statement: 24**3** + 71 words
- Introduction: **838** words
- Discussion: **1779** words

CONFLICT OF INTEREST:
AJL, ER, and ARP are inventors of the cSNAIL patent. Other authors do not declare any conflict of interest.

ACKNOWLEDGEMENT:
We would like to thank members of the Eric Yttri lab at Carnegie Mellon University for providing *Drd1-cre* and *Adora2a-cre* mice for cell type-specific ATAC-seq experiments.

Author contributions: Conceptualization: ARP, BNP, CS; ATAC-seq data processing: AJL, ER, IMK, BNP; GWAS enrichment investigation: BNP, CS, ER, MK; Machine learning models: AJL, BNP, ER, IMK; bulk tissue ATAC-seq: AJL, ARB, MEW; cSNAIL ATAC-seq: AJL, ARB; writing (original draft): BNP, CS; review and editing: AJL, ARP, BNP, CS, ER, IMK; funding acquisition, resources, & supervision: ARP;

Funding: National Institute of General Medical Sciences training grant T32GM008208 (BNP), National Institute On Drug Abuse of the National Institutes of Health Award Number F30DA053020 (BNP). Sloan Foundation Fellowship (ARP), National Institute on Drug Abuse Avenir Award 1DP1DA046585 (ARP), National Science Foundation Graduate Student Research Fellowship DGE1745016 (AJL), Carnegie Mellon Brainhub Presidential Fellowship (ER), Carnegie Mellon Computational Biology Department Lane Postdoctoral Fellowship (IMK)

ABSTRACT

Recent large genome-wide association studies (GWAS) have identified multiple confident risk loci linked to addiction-associated behavioral traits. Genetic variants linked to addiction-associated traits lie largely in non-coding regions of the genome, likely disrupting cis-regulatory element (CRE) function. CREs tend to be highly cell type-specific and may contribute to the functional development of the neural circuits underlying addiction. Yet, a systematic approach for predicting the impact of risk variants on the CREs of specific cell populations is lacking. To dissect the cell types and brain regions underlying addiction-associated traits, we applied LD score regression to compare GWAS to genomic regions collected from human and mouse assays for open chromatin, which is associated with CRE activity. We found enrichment of addiction-associated variants in putative **CREs** marked by open chromatin in neuronal (NeuN+) nuclei collected from multiple prefrontal cortical areas and striatal regions known to play major roles in reward and addiction. To further dissect the cell type-specific basis of addiction-associated traits, we also identified enrichments in human orthologs of open chromatin regions of mouse **neuronal subtypes: cortical excitatory, D1, D2, and PV**. Lastly, we developed machine learning models from mouse cell type-specific regions of open chromatin to further dissect human NeuN+ open chromatin regions into cortical excitatory or striatal D1 and D2 neurons and predict the functional impact of addiction-associated genetic variants. Our results suggest that different **neuronal subtypes** within the reward system play distinct roles in the variety of traits that contribute to addiction.

Significance Statement:

We combine statistical genetic and machine learning techniques to find that the predisposition to for nicotine, alcohol, and cannabis use behaviors can be partially

explained by genetic variants in conserved regulatory elements within specific brain regions and neuronal subtypes of the reward system. This computational framework can flexibly integrate **open chromatin** data across species to screen for putative causal variants in a cell type- and tissue-specific manner across numerous complex traits.

INTRODUCTION

Substance use disorders (SUD) have increased in prevalence over the last three decades, with an estimated 100 million cases worldwide (GBD 2016 Alcohol and Drug Use Collaborators, 2018; Eddie et al., 2019). Pharmacological interventions are limited in their ability to cure addiction due to physiological and logistical barriers (Pullen and Oser, 2014; Pear et al., 2019). As the societal epidemic of substance use grows, there is a greater need to understand the neurobiology of substance use behaviors and addiction.

The reward circuits co-opted in addiction **as well as the associated neural cell types** are highly conserved across primates and rodents **(Monaco et al., 2015; Grillner and Robertson, 2016; Scaplen and Kaun, 2016; Hodge et al., 2019)**. It is generally accepted that addictive substances promote impulsive and compulsive behavior by activating the mesolimbic dopamine system, in which dopaminergic inputs from the ventral tegmental area project to medium spiny neurons (MSN) of the nucleus accumbens (NAc) **in the ventral striatum (STR)** (Koob and Volkow, 2010). Glutamatergic inputs to the NAc from the amygdala, frontal cortex, and hippocampus contribute to motivational action through the extrapyramidal motor system (Koob and Volkow, 2010). Subsequently, the NAc sends outputs to nuclei of the ventral pallidum**, which are** critical for processing and modulating substance reward signal (Koob and Volkow, 2010). **The development of compulsive substance-seeking is hypothesized to be linked to recruitment of the dorsal STR, which together with the prefrontal cortical regions regulates a variety of reward and addiction-related phenotypes** (Koob and Volkow, 2010; Goldstein and Volkow, 2011). **These** findings emphasize **that substance abuse behavior involves** the interplay of **the** brain regions and **cell types that make up the reward system.**

95 Increasing evidence reveals strong genetic links to substance use risk (Pasman et al.,
96 2018; Erzurumluoglu et al., 2019; Karlsson Linnér et al., 2019; Liu et al., 2019b) and SUD
97 (Kendler and Prescott, 1998a, 1998b; Dick, 2016; Waaktaar et al., 2018). Genome-wide
98 association studies (GWAS) report that genetic risk for substance use shares underlying
99 architecture with other neuropsychiatric disorders (Pasman et al., 2018; Liu et al., 2019b), of
100 which risk variants tend to lie in non-coding, functional regions of the human genome (Jensen,
101 2016). These **genetic variants, including** single nucleotide polymorphisms (SNPs), can disrupt
102 transcription factor binding in cis-regulatory elements (CREs) with varying impact on gene
103 regulation and downstream neural circuitry. Many CREs have tissue- and cell type-specific
104 activity (Roadmap Epigenomics Consortium et al., 2015), suggesting that cell types and tissues
105 underlying addiction may be uniquely targeted by genetic variants at these CREs. GWAS for
106 nicotine-, alcohol- (Liu et al., 2019b), and cannabis-use traits (Pasman et al., 2018) have
107 identified multiple confident risk loci and SNPs linked to addiction-associated phenotypes with
108 brain-specificity, yet their effects on the CREs of specific brain regions and cell types involved
109 in addiction pathophysiology are an open area of inquiry.

110 **A comparison of GWAS to functional annotations of the human genome** have
111 **yielded estimates that over 90% of SNPs associated with complex phenotypes lie** within
112 functional non-coding regions**, which are marked by epigenetic features including open**
113 **chromatin. (Maurano et al., 2012; Finucane et al., 2015)**. Linkage disequilibrium (LD) of
114 significant SNPs complicates the identification of causal variants contributing to genetic risk
115 (Bush and Moore, 2012). **Regression of SNP LD scores against GWAS summary statistics**
116 **(LDSC regression) is the dominant method for relating human genetics to functional**
117 **annotations. LDSC regression partitions risk SNPs identified by GWAS into the tissues or**

118 **cell types in which genetic variation in CREs may contribute to heritability of complex**
119 **traits (Finucane et al., 2015; Visscher et al., 2017)**. **Yet**, the functional consequences of risk
120 SNPs in CRE sequences cannot be reliably inferred from DNA sequences alone (Shlyueva et al.,
121 2014). Recent developments in epigenomic assays (Buenrostro et al., 2013; Mo et al., 2015; Tak
122 and Farnham, 2015) and machine learning (Ghandi et al., 2014; Zhou and Troyanskaya, 2015;
123 Kelley et al., 2016, 2018; Lee, 2016) can predict cell types affected by addiction-associated
124 genetic variation to propose cell type-specific hypotheses on the pathogenesis of addiction.

125 Here, we implement a framework that **links the genetic predisposition to addiction-**
126 **associated traits to specific brain** regions and cell types **within them by identifying which**
127 **have open chromatin regions that are enriched for SNPs identified by GWAS**. We first
128 **intersect SNPs measured by GWAS** across human and mouse bulk tissue and cell type-specific
129 open chromatin **regions** to identify **putative** region- and cell type-specific CREs that may be
130 impacted by genetic variation associated with addiction-related traits. **To overcome limits of**
131 **cellular resolution in the human brain, we apply convolutional neural network models**
132 **trained on transgenically-labelled neuron populations in the reward system of mice to**
133 **predict the cell type-specificity of GWAS-associated SNPs in the human genome. We**
134 **further** apply these models to **the problem of** screen**ing** for putative causal SNPs within dense
135 loci reported in GWAS for addiction-associated traits. This pipeline, to our knowledge, describes
136 the first integrative analyses across species, **brain** regions and cell types to screen for candidate
137 causal addiction-associated genetic risk variants in dense loci with numerous significant SNPs in
138 LD.

139 **RESULTS**

140 **Genetic risk for substance use traits is associated with the neuronal epigenomes of reward**
141 **areas**

142 Recent well-powered GWAS have **identified dozens of candidate genetic risk loci**
143 **associated with seven addiction-associated traits: age of smoking initiation**
144 **(`AgeOfInitiation`), average number of cigarettes smoked per day**
145 **(`CigarettesPerDay`), having ever regularly smoked (`SmokingInitiation`), being a**
146 **former versus current smoker (`SmokingCessation`), the number of alcoholic drinks**
147 **per week (`DrinksPerWeek`), and lifetime cannabis use (`Cannabis`), and risk tolerance**
148 **(`RiskyBehavior`)** (Pasman et al., 2018; Karlsson Linnér et al., 2019; Liu et al., 2019b). These
149 GWAS **measure** reward, risk tolerance, and various substance use behaviors**, thereby providing**
150 a means of studying genetic variation associated with addiction. We found that 72-98% of
151 addiction-associated genetic variants **lie in** non-coding regions of the genome **(Figure 1A)**. **Of**
152 **those risk variants, 47-85% lie in introns, which is a substantial over-representation in each**
153 **GWAS** (odds ratio, $OR_{AgeOfInitiation}$ =2.3, $OR_{Cannabis}$ = 2.3, $OR_{CigarettesPerDay}$ = 1.4, $OR_{DrinksPerWeek}$ =
154 1.6, $OR_{RiskyBehavior}$ = 1.4, $OR_{SmokingCessation}$ = 1.8, $OR_{SmokingInitiation}$ =1.3, Fisher's Exact $P_{Bonferroni}$ <
155 8×10^{-79}). Furthermore, **pairwise genetic correlations of risk alleles in these seven GWAS**
156 **indicated shared and distinct genetic architecture across addiction-associated traits** (r_g,
157 **Supplemental Figure 1A**). Although common genetic variants are shared between addiction-
158 associated traits on a genome-wide scale, the reported significant loci are often unique to a
159 particular trait and are densely packed with SNPs in high LD **(Supplemental Figure 1B**). **SNPs**
160 **that are associated with the seven traits span 205 non-overlapping loci across the human**
161 **genome and include on average 71 SNPs (minimum 1, median 22.5, maximum 1780) within**

162 **each locus that are either genome-wide significant ($P_{GWAS} < 5 \times 10^{-8}$) or in high LD with the**
163 **lead SNPs ($R^2 > 0.8$, Supplemental Table 1).**

164 We investigated whether genetic variants **implicated by** addiction-associated GWAS
165 **show a tendency to** cluster at putative cis-regulatory elements (CREs) of the brain using a
166 partitioned heritability LDSC regression approach**, which looks for an enrichments of**
167 **significant SNPs from GWAS in human annotations** (Bulik-Sullivan et al., 2015b; Finucane
168 et al., 2018). **We applied LDSC to compare the seven addiction-associated GWAS to** open
169 chromatin region (OCR) annotations of sorted neuronal (NeuN+) and glial (NeuN-) nuclei across
170 14 brain regions(Fullard et al., 2018) **(Figure 1B)**. We found that genetic variants associated
171 with `SmokingInitiation`, `SmokingCessation`, `DrinksPerWeek`, and `Cannabis`
172 significantly enriched in NeuN+ OCRs of brain regions known and speculated to contribute to
173 reward and addiction(Volkow and Morales, 2015) (FDR < 0.05). **We** found that genetic variants
174 associated with `SmokingInitiation` and `Cannabis` shared enrichment in NeuN+
175 prefrontal cortical OCRs (from orbitofrontal cortex and dorsolateral prefrontal cortex) while
176 those associated with `SmokingCessation` and `DrinksPerWeek` shared enrichment in
177 NeuN+ striatal OCRs (both putamen and NAc). The enrichments of NeuN+ OCRs indicate that
178 genetic variation in epigenomes of neuronal populations from frontal cortex and striatum
179 contribute to addiction liability. The difference in NeuN+ enrichments between regions across
180 addiction-associated traits can likely be explained by the difference in proportions **and identities**
181 of neuronal subtypes of each area, so we sought to dissect the different neuronal subtypes
182 contributing to these enrichments.

183 Broad marker-gene based labeling approaches, such as using NeuN to label neurons, do
184 not capture the rich diversity of neuronal subtypes; bulk NeuN+ open chromatin signal

185 represents an average signal from heterogeneous neuronal subtypes, each with distinct
186 epigenomic landscapes, gene regulation, network connectivity. Hence, NeuN-labeled open
187 chromatin profiles likely do not capture OCRs unique to less populous neuronal subtypes. The
188 difference in proportions of neuronal subtypes between brain regions may also contribute to
189 brain region-specific NeuN+ OCR enrichment for GWAS variants of addiction-associated traits.
190 We therefore applied LDSC regression GWAS enrichment on **single cell** open chromatin profiles
191 from human postmortem **isocortical, striatal, hippocampal, nigral (Figure 1C) and occipital**
192 **cortical cell types** (Lake et al., 2018; Corces et al., 2020) **(Figure 1D)**. We found that addiction-
193 associated genetic variants largely enriched in both excitatory and inhibitory neuronal OCRs.
194 **Genetic variants associated with `SmokingInitiation`, `SmokingCessation`,**
195 **`DrinksPerWeek`, and `Cannabis` enriched in isocortical excitatory neuron OCRs**
196 **(Figure 1C). We found enrichment of genetic variants associated with**
197 **`CigarettesPerDay`, `SmokingInitiation`, `SmokingCessation`,**
198 **`DrinksPerWeek`, `Cannabis`, and `RiskyBehavior` in striatal inhibitory neurons.**
199 **Genetic variants associated with `Cannabis` also enriched in isocortical inhibitory neuron**
200 **and unclassified neuron OCRs. Among the glial cell types, only oligodendrocyte precursor**
201 **cell OCRs were enriched for an addiction-associated trait (`SmokingInitiation`).** We
202 found enrichment of genetic variants associated with `AgeOfInitiation` and
203 `SmokingCessation` in OCRs of **occipital** cortical excitatory neurons. We found no
204 enrichment of genetic variants associated with `CigarettesPerDay` for OCRs of occipital
205 cortex cell types. Genetic variants associated with `SmokingInitiation`, which enriched in
206 astrocyte, endothelial, inhibitory, and oligodendrocyte precursor cell OCRs **from occipital**
207 **cortex**, shared enrichment in NeuN- OCRs of mediodorsal thalamus **(Figure 1B)**. Interestingly,

208 genetic variants associated with SmokingCessation, which **showed enrichment** for striatal
209 NeuN+ OCRs, enriched only for OCRs of **occipital** cortical excitatory neurons and not cortical
210 inhibitory neurons. Sorted bulk ATAC-seq only showed enrichment of SmokingCessation
211 associated genetic variants in OCRs of NeuN+ striatal regions, which are largely composed of
212 inhibitory MSNs. **We overall found that the enrichments of addiction-associated genetic**
213 **variants in Corces *et al.* isocortex OCRs agreed with those in Lake *et al.* occipital cortex**
214 **OCRs**. Single-cell epigenomics of human postmortem brain can further dissect the genetic risk
215 for substance-use traits into neuronal subtypes that otherwise would not be parsed with bulk
216 tissue assays.

217 We confirmed that our pipeline for LDSC regression on NeuN-sorted OCRs from 14
218 brain regions is able to reproduce the GWAS enrichments published by Fullard *et al.* While our
219 approach uses OCRs from reproducible ATAC-seq peaks rather than differentially accessible
220 peaks, we found consistent enrichments of genetic variants associated with schizophrenia risk
221 (Schizophrenia), highest level of educational attainment (EduAttain), and habitual
222 sleep duration (SleepDuration) **(Supplemental Figure 2B)**. We did not find enrichment in
223 brain OCRs of genetic variants identified in several low-powered GWAS (cocaine dependence
224 (CocaineDep) (Cabana-Domínguez et al., 2019), opioid dependence (OpioidDep) (Cheng
225 et al., 2018), and obsessive-compulsive disorder (OCD) (International Obsessive Compulsive
226 Disorder Foundation Genetics Collaborative (IOCDF-GC) and OCD Collaborative Genetics
227 Association Studies (OCGAS), 2018), each of which had included fewer than 5000 individuals
228 with the trait **(Supplemental Figure 2A)**. In addition, we found no enrichments in brain OCR
229 for several well-powered studies of traits related to addiction behaviors, **including** multi-site
230 chronic pain (ChronicPain) (Johnston et al., 2019) and cups of coffee per day

231 (CoffeePerDay) (Coffee and Caffeine Genetics Consortium et al., 2015). We also found no
232 enrichment in brain OCRs for anthropometric traits, **including** coronary artery disease (CAD)
233 (Howson et al., 2017), bone mineral density (BMD) (Kemp et al., 2017), and lean body mass
234 (LBM) (Zillikens et al., 2017) **(Supplemental Figure 2B, C)**. Lastly, we validated that human
235 OCRs from non-brain tissues would not enrich for risk variants associated with brain traits. We
236 gathered publicly available OCRs from stomach ATAC-seq, adipocyte ATAC-seq, preadipocyte
237 ATAC-seq, liver DNase-seq, and lung DNase-seq profiles (ENCODE Project Consortium, 2012;
238 Thurman et al., 2012; Davis et al., 2018; Cannon et al., 2019) **(Supplemental Figure 4D)** and
239 performed LDSC regression on the total 18 GWAS from above. To our expectation, we did not
240 find enrichments of stomach, liver, or lung OCRs for genetic variants associated with brain-
241 related traits. We did find enrichment of BMD in lung OCRs, a connection previously recognized
242 (Lee et al., 2016; Kim et al., 2019; Zeng et al., 2019). The secondary GWAS enrichments in
243 other traits and foregrounds demonstrate two trends: a GWAS trait would enrich if the GWAS
244 was properly powered to detect genetic risk variants, and the foreground regions are from cell
245 types or tissue of that trait's potential etiological origin.
246
247 **Mouse-human conserved cell type-specific open chromatin enrich for addiction risk loci**
248 In order to **further interrogate the** different neuronal subtypes that comprise the
249 enrichment **of addiction-associated genetic variants in OCR sets measured by Fullard *et al.*,**
250 **Lake *et al.*, and Corces *et al.* (Figure 1, Supplemental Figure 2)**, we performed targeted
251 epigenomic **experiments** in mouse **on isolated neuronal subtypes** from **key brain regions of**
252 **the reward circuit:** frontal cortex (CTX), caudoputamen (CPU), and the nucleus accumbens
253 (NAc). We isolated **nuclei from specific cell types** for ATAC-seq using a modified version of

254 the INTACT approach (Mo et al., 2015) **called** *cre*-specific nuclei anchored independent labeling
255 (cSNAIL). cSNAIL-INTACT **was applied** to isolate nuclei marked by *Pvalb*, *Sst*, *Drd1*, and
256 *Adora2a* **in *cre-driver*** lines **using a shortened form of the *Sun1-Gfp* fusion protein packaged**
257 **with AAV-PHP.eb and delivered through retro-orbital injection (Figure 2A)**. We show that
258 cell type-targeting provided markedly distinct genome-wide ATAC-seq profiles compared to
259 bulk tissue ATAC-seq alone (**Supplemental Figure 3A**). cSNAIL ATAC-seq specifically
260 captured nuclei with increased accessibility around the marker gene that was driving *Cre*
261 recombinase expression (**Supplemental Figure 3B**). Accessibility around cSNAIL ATAC-seq
262 transcription start sites (TSS) strongly correlated with matched pseudobulk gene expression in
263 the same cell type and tissue (**Methods**, both Pearson and Spearman correlation $P_{bonf} < 2 \times 10^{-16}$,
264 **Supplemental Figure 3C,D**). We applied HALPER**, an approach that leverages reference-**
265 **free multi-species genome alignments to produce 1-1 contiguous CRE orthologs** (Zhang et
266 al., 2020), to reliably map ~70% of mouse **neuronal subtype** OCRs to their human orthologs in
267 **the hg38 human reference genome (Methods) for LDSC regression GWAS analysis**.
268 Our GWAS enrichment **analysis** of human orthologs from mouse OCRs **(mouse-human**
269 **orthologs) measured in** various neuronal subtypes and bulk tissue **(Figure 2B)** show that
270 genetic variants associated with `SmokingInitiation` and `Cannabis` shared enrichment in
271 cortical PV and EXC neuron OCRs from both Mo *et al.* and this study (**Pfenning data,** FDR <
272 0.05). **Genetic variants associated with `Cannabis`** further enriched in CTX bulk tissue OCRs,
273 which could be attributed to signal from cortical EXC and PV neuron populations. Cortical PV
274 neuron OCRs further enriched with genetic variants associated with `DrinksPerWeek`.
275 `SmokingCessation` associated genetic variants distinctly enriched in cortical VIP neuron
276 OCRs.

277 Within **neuronal subtypes** from CPU and NAc, we found enrichment of genetic variants
278 associated with all measured addiction-associated traits in CPU and NAc D2 MSN OCRs.
279 Genetic variants associated with all measured traits excluding `SmokingInitiation` and
280 `RiskyBehavior` all enriched in CPU and NAc D1 MSN OCRs. CPU D1 MSN OCRs were
281 enriched with genetic variants associated with all measured traits excluding `RiskyBehavior`.
282 We found that CPU bulk tissue OCRs were enriched with genetic variants associated with all
283 measured addiction-associated traits excluding `AgeOfInitiation` and `RiskyBehavior`.
284 Distinctly, CPU PV+ and SST+ neuron OCRs enriched with genetic variants associated with
285 `Cannabis`.

286 Corresponding to our analysis of human brain OCRs, we also confirmed the specificity of
287 mouse-human orthologous CRE enrichments for genetic variants **associated with** addiction-
288 related, brain-related, and non-brain related traits **(Supplemental Figure 4)**. We found
289 enrichments of genetic variants associated with `ChronicPain` in cortical PV neuron OCRs
290 from both Mo *et al.* and this study **(Supplemental Figure 4A).** Within striatal cell types, we
291 found that CPU D2 and NAc D1 MSN OCRs were enriched for genetic variants associated with
292 `ChronicPain`. In contrast, CPU D1 and NAc D2 MSN OCRs were enriched for genetic
293 variants associated with `OpioidDep`. Genetic variants associated with `OpioidDep` also
294 enriched in CPU D1 MSN and CPU PV OCRs. `Schizophrenia`, `EduAttain`, and
295 `SleepDuration` associated genetic variants all enriched in OCRs of all measured cell types
296 **(Supplemental Figure 4B)**. None of these **mouse-**human orthologs enriched for genetic variants
297 associated with non-brain-related traits: `BMD`, `CAD`, and `LBM` **(Supplemental Figure 4C)**. We
298 validated that our approach to map OCRs from mouse to human did not bias enrichment to brain
299 traits by performing GWAS enrichment on OCRs from mouse non-brain tissues (kidney, liver,

300 and lung) (**Supplemental Figure 4D)**. As expected, we did not find an enrichment for genetic
301 variants associated with a brain-related trait. We did find that **mouse-**human orthologs of lung
302 OCRs enrich for BMD, which concords with the enrichment of human lung OCRs.
303
304 **Convolutional Neural Network (CNN) models of mouse cell type-specific CRE activity**
305 **refine human NeuN+ OCRs for GWAS enrichment**
306 **The genetic tools available for mouse research allowed us to isolate the nuclei of**
307 **specific neuronal subtypes and generate deep open chromatin profiles at greater cellular**
308 **resolution. However, a lack of mouse-human conservation in the cell type-specificity of**
309 **CREs could lead to false negatives and false positives at specific loci that add noise to**
310 **GWAS comparisons. To leverage the strengths of the mouse and human approaches, we**
311 **developed a procedure to predict the neuronal subtype-specificity of human OCRs using**
312 **machine learning models trained in mouse. The OCR profile of each neuronal subtype is a**
313 **result of a developmental cascade of transcription factors that cooperatively recognize and**
314 **bind to specific sequence elements in the genome, resulting in a neuronal subtype-specific**
315 **open chromatin profile** (Spitz and Furlong, 2012). **These complex combinations of sequence**
316 **features comprise regulatory code that links genome sequence to neuronal subtype-specific**
317 **open chromatin. This regulatory code can be effectively learned using convolutional neural**
318 **networks (CNNs) and has been demonstrated to be highly conserved between mouse and**
319 **human** (Zhou and Troyanskaya, 2015; Chen et al., 2018)
320 The concordant pattern of enrichment for addiction associated genetic variants in human
321 and mouse-human orthologous OCRs suggested that risk variants may affect the regulatory
322 **activity of neuronal subtypes** conserved **between human and** mouse. We therefore **devised**

323 **and trained a collection of CNN binary classification models to learn the genome sequence**
324 **features that distinguish OCRs** for cortical excitatory (EXC) neurons, striatal D1 MSNs, and
325 striatal D2 MSNs (Zhou and Troyanskaya, 2015; Kelley et al., 2016, 2018; Chen et al., 2018).
326 For each set of reproducible OCRs from mouse INTACT and cSNAIL group, we trained 5-fold
327 cross-validated models to predict the reproducible peaks from ten times the number of
328 **nucleotide content**-matched negative sequences **(Methods)**. Our models made confident
329 predictions on held-out test sequences as reported by **high F1-scores, high area under the**
330 **precision-recall curves (Supplemental Figure 5A)**, **and low false positive rates at a blind**
331 **threshold of 0.5 (Supplemental Figure 5B). These models reproducibly learned**
332 **transcription factor motif families that are enriched in human neuronal subtypes of cortex**
333 **(MEF2, JUN) and striatum (POU, NRF1, ZFHX3), as previously reported by Fullard *et al.***
334 **(Supplemental Figure 5F, Supplemental Table 2)**.
335 We reasoned that NeuN+ OCR signal**, which is comprised of OCR signals from**
336 **several neuronal subtypes, can be parsed into its component cell types by CNNs that are**
337 **trained to predict OCR activity in those component cell types**. **This enables the study of**
338 **human addiction genetics at a cell type-level resolution from high-quality tissue-level open**
339 **chromatin profiles**. To discern whether NeuN+ OCR enrichments in addiction-associated
340 genetic variants come from the same cell types **observed** in **Figure 3**, we **applied our trained**
341 **CNN** models to predict whether **bulk** cortical or striatal NeuN+ OCRs have activity in **either**
342 cortical EXC or striatal D1 and D2 **neurons**, respectively **(Figure 3A)**. We did not conduct these
343 analyses for PV neurons because they comprise a much lower percentage of cortical and striatal
344 neurons than the other neuron types (Beaulieu, 1993; Lefort et al., 2009). We ran LDSC
345 regression (Finucane et al., 2018) GWAS enrichments on the sets of NeuN+ OCRs predicted to

346 be specific to cortical EXC, striatal D1, and striatal D2 neurons. Genetic variants associated with
347 `SmokingInitiation`, which initially enriched in OCRs of various NeuN+ frontal cortical
348 areas **(Figure 1B)**, enriched in NeuN+ OCRs predicted to be active in EXC neurons **(Figure**
349 **3B)**. Genetic variants associated with `Cannabis`, which enriched in NeuN+ cortical OCRs
350 **(Figure 1B)**, also enriched in NeuN+ OCRs predicted to be active in EXC neurons. The
351 enrichments of excitatory cortical cell type-specific OCRs for `SmokingInitiation` and
352 `Cannabis` associated genetic variants agree with the results from the **analysis of the** Fullard *et*
353 *al*.**, Corces et al., and** Lake *et al*. **OCR** datasets **(Figure 1B, C)**. Genetic variants associated
354 with `SmokingCessation` and `DrinksPerWeek`, which enriched in PUT and NAc NeuN+
355 OCRs **(Figure 1B)**, shared enrichment in OCRs predicted active in both D1 and D2 MSNs of
356 both PUT and NAc. The framework that we outline in **Figure 3A** refines addiction genetic risk
357 signal to neuronal subtypes **and** maintains the brain region context of the source NeuN+ OCR.
358 **This framework can be applied to CREs from any tissue-cell type combination for which**
359 **bulk tissue open chromatin measurements are available from human and cell type open**
360 **chromatin measurements are available from another vertebrate** (Chen et al., 2018; Minnoye
361 et al., 2020).
362

363 **Convolutional Neural Network (CNN) models predict allele-specific activity of addiction-**
364 **associated GWAS SNPs in neuronal subtypes**

365 Lastly, we applied our convolutional neural network (**CNN)** models to screen addiction-
366 associated genetic variants for predicted functional activity in EXC, D1, and D2 neuronal
367 subtypes. **CNN**-based approaches have been demonstrated to fine-map dense risk loci and select
368 candidate causal genetic variants (Alipanahi et al., 2015; Zhou and Troyanskaya, 2015; Kelley et

369 al., 2016, 2018; Corces et al., 2020), yet none have been applied in the context of addiction-
370 associated genetic risk or in the cell types that we have assayed. **We identified 14,790 unique**
371 **SNPs that were collected across the seven addiction-associated GWAS to score for**
372 **differential neuronal subtype OCR activity (Methods)**. **We expect that many SNPs reported**
373 **from GWAS are significantly associated with traits due to LD rather than being the true**
374 **causal variant. When scored with our CNN models, the 96.2% of addiction-associated**
375 **SNPs that either do not lie in any OCR or in only NeuN- OCR have low probability to be**
376 **active in excitatory, D1, or D2 neuronal subtypes. We also found that these SNPs have**
377 **significantly lower predicted probability of activity than the remaining 3.8% of addiction-**
378 **associated SNPs in any NeuN+ OCR ($P_{Bonferroni} < 0.05$, Figure 4A). We then predicted the**
379 **probability of activity for both the effect and non-effect allele and estimated the differential**
380 **impact of the alleles in order to fine-map candidate causal effect SNP and target neuronal**
381 **subtype and tissue. Most SNPs do not have predicted differential allelic activity in a**
382 **neuronal subtype, while a handful of SNPs have larger differential activity that deviate**
383 **from a normal distribution when visualized on quantile-quantile plots (Supplemental**
384 **Figure 5C, Methods). We outline in Supplemental Figure 5D an approach to prioritize the**
385 **candidate causal SNPs by two lines of evidence: 1) a predicted differential neuronal**
386 **subtype OCR activity with large effect size that is controlled for false discovery (q-value <**
387 **0.05, Methods) and 2) having physical overlap with measured human NeuN+ OCR in**
388 **Fullard *et al.* (Supplemental Figure 5D). We are able to prioritize 55 SNPs spanning 37 loci**
389 **to Tier A which have both significant predicted ΔSNP probability effect and overlaps a**
390 **Fullard *et al.* NeuN+ OCR, 505 SNPs to Tier B that only have predicted ΔSNP probability**

391 **effect, and 502 SNPs to Tier C as overlapping NeuN+ open chromatin without a predicted**
392 **significant ΔSNP probability effect (Supplemental Table 1).**
393 One such SNP **from Tier A**, rs7604640, lies in **human** NeuN+ open chromatin specific
394 to striatum 46kb upstream of the *SIX3* locus on chromosome 2. rs7604640 overlaps human
395 orthologs of mouse OCRs in only D1 and D2 neurons and **we predict the effect allele of**
396 **rs7604640 has an increased probability of open chromatin activity in D1 OCRs of the**
397 **striatum compared to the non-effect allele (Figure 4B)**. rs7604640 is one of many off-lead
398 SNPs identified in the `SmokingInitiation` GWAS (P_{GWAS} =3.04 x 10^{-12}) and is in **high** LD
399 with the SNP rs163522 **(R^2 = 0.856, P_{GWAS} =1.11 x 10^{-11}), which is independently significant**
400 **from the lead SNP, rs1004787 (R^2 = 0.630, P_{GWAS} =5.27 x 10^{-17}). rs7604640 was reported by**
401 **HaploRegv4 to overlap a POU1F1 motif** (Ward and Kellis, 2016)**, which our D1 models**
402 **predict to contribute towards increased probability of being active in D1 MSNs (Figure**
403 **4C).** Furthermore, this SNP is a known *cis*-eQTL for the antisense *SIX3-AS1* gene in striatal
404 regions from the Genotype-Tissue Expression (GTEX) project (GTEx Consortium, 2013, 2015;
405 Melé et al., 2015; GTEx Consortium et al., 2017). Anti-sense gene expression is one mechanism
406 of regulating their sense gene (Pelechano and Steinmetz, 2013; Barman et al., 2019), and
407 deletion of the gene *SIX3* has been shown to inhibit development of D2 medium spiny neurons
408 (Xu et al., 2018). Altogether, this evidence formulates the hypothesis that common genetic
409 variant rs7604640 has D1 MSN-specific**, allelic impact on** open chromatin activity in a mouse-
410 human conserved putative CRE regulating the MSN regulator *SIX3*.
411 **In addition to rs7604640, we report four loci with 1-4 candidate SNPs each in Tier A** that
412 may be putative causal SNPs with cell type-specific activity in addiction-associated traits
413 **(Supplemental Figure 6)**. **The SNPs in these loci all have reported eQTL in frontal cortex**

414 **or striatum tissues from GTEx, and they overlap corresponding NeuN+ OCRs and mouse-**
415 **human orthologous OCRs. In some cases, our prioritized Tier A SNPs were predicted to**
416 **have ΔSNP effects (Methods) in only striatal MSNs, showcasing our framework's ability to**
417 **predict cell type-specific impact. These SNPs include rs11191352 ($P_{SmokingInitiation}$=2.12 x 10^{-}**
418 **^{7}, Supplemental Figure 6A), rs9826458 ($P_{RiskyBehavior}$= 4.36 x 10^{-21}, $P_{SmokingInitiation}$=1.21 x 10^{-}**
419 **^{14}, Supplemental Figure 6B), and rs9844736 ($P_{RiskyBehavior}$= 3.04 x 10^{-7}, $P_{SmokingInitiation}$=3.58 x**
420 **10^{-7}, Supplemental Figure 6C). In a few cases, our models predicted SNPs to have strong**
421 **ΔSNP effects across both cortical excitatory and striatal cell types. These include two SNPs**
422 **in the highly pleiotropic MAPT-CRHR1 locus that are 152bp apart and in perfect LD with**
423 **each other, rs11575895 and rs62056779 (Supplemental Figure 6D). The prioritized SNPs in**
424 **the MAPT-CRHR1 locus are genome-wide significant for 5 of the 7 addiction-associated**
425 **traits (Supplemental Table 1) and the locus has been implicated in other neuropsychiatric**
426 **traits such as Alzheimer's Disease (Hoffman et al., 2019; Corces et al., 2020; Ramamurthy**
427 **et al., 2020). We provide the summary of CNN predictions in these reported loci across all**
428 **14,790 analyzed SNPs along with the accompanying annotations that we incorporated into**
429 **our prioritization of candidate causal SNPs and their predicted cell types (Supplemental**
430 **Table 1).**

431 **DISCUSSION**

432 In this study, we demonstrate the first analyses integrating **neuronal subtype** OCRs
433 across human and mouse brain epigenomics using **CNN** models to select candidate addiction-
434 associated SNPs acting at putative **neuronal subtype**-specific CREs. We trained **CNN** models to
435 predict **neuronal subtype**-specific activity of OCRs and used the models to predict whether
436 addiction-associated genetic variants in risk loci impact putative CRE function. Our findings link
437 the genetic heritability of addiction-associated behaviors to the OCR profiles of **neuronal**
438 **subtypes** and brain regions and present specific hypotheses describing how genetic variants may
439 impact gene regulation in addiction-associated behaviors. These analyses in conjunction suggest
440 that genetic variation-associated nicotine, alcohol, and cannabis use behaviors may impact
441 putative CREs in different combinations of excitatory (EXC), D1, and D2 neuronal subtypes.
442 These findings provide a foundation for future investigations into the cell type-specific genetic
443 mechanisms underlying addiction-related traits. More broadly, our cross-species integrative
444 computational framework leverages high-resolution cell-type targeted epigenomics in model
445 organisms to interpret the genetic risk variants of complex traits in humans.

446 We initially found that addiction-associated genetic variants were enriched in human
447 NeuN+ OCRs of the prefrontal cortex and striatum, known areas involved in addiction and
448 reward circuitry (Volkow et al., 2013; Koob and Volkow, 2016) **(Figure 5A)**. Genetic variants
449 associated with `SmokingInitiation` and `Cannabis`, initiating behaviors of substance use,
450 were enriched in NeuN+ OCRs of prefrontal areas including DLPFC, VLPFC, and OFC **(Figure**
451 **1B)**. These OCRs were predicted to be active in cortical excitatory neurons of these brain regions
452 **(Figure 3B)**. Addiction-associated genetic variants that enrich in OCRs of cortical excitatory
453 neurons in these areas may reduce corticostriatal activation from prefrontal cortex to inhibit

454 behaviors predisposing the initiation of substance use (Koob and Volkow, 2010, 2016; Volkow
455 et al., 2013; Volkow and Morales, 2015). These genetic variants may contribute to reduced
456 prefrontal self-control reward, leading to behaviors observed in addiction such as impulsivity,
457 reduced satiety, and enhanced motivation to procure drugs (Volkow et al., 2013; Volkow and
458 Morales, 2015). In addition, we found enrichment of striatal NeuN+ OCRs for genetic variants
459 associated with `SmokingCessation` and `DrinksPerWeek` **(Figure 1B)**. In **Figure 3B**, we
460 showed that these genetic variants are predicted to affect open chromatin in both D1 and D2
461 MSNs, which are coordinators of mesocorticostriatal dopamine systems (Koob and Volkow,
462 2010, 2016; Volkow et al., 2013). Genetic variants affecting open chromatin in these MSN
463 subtypes may predispose individuals to increased alcohol use (`DrinksPerWeek`) or decreased
464 nicotine use (`SmokingCessation`), perhaps driving the neuroplastic changes in D1 and D2
465 MSNs observed in human and rodent drug dependence studies (Volkow et al., 1996, 1997, 2003;
466 Wang et al., 1997; Fehr et al., 2008; Cheng et al., 2017; Wilar et al., 2019). While drug addiction
467 has been attributed to various areas of the reward circuit, our investigations into heritable genetic
468 risk for addiction-associated traits unravel how regulatory DNA sequence variation in OCRs of
469 projection neurons in implicated areas link genetic risk to neural circuits to behavior.

470 Since **key component cell types of the reward circuit such as D1 and D2 MSNs have**
471 **not been profiled for high-quality open chromatin measurements in a human reference**
472 **genome to our best knowledge, we leveraged high-quality mouse cell type open chromatin**
473 **measurements using a cross-species OCR mapping framework. We first** conducted ATAC-
474 seq of **MSN** and interneuron subtypes in mouse brain **to identify neuronal subtype-specific**
475 **OCRs. Then, we used a multiple genome sequence alignment framework to identify the**
476 **orthologous regions of the human genome.** By leveraging **reference-genome free CRE**

477 ortholog mapping tools, we retained high-quality cell type-specific measurements within relevant
478 brain regions of the reward circuit, enabling analysis of cell populations from brain regions
479 where we lack primary human open chromatin profiles. Across these brain regions, we found
480 remarkably concordant enrichments of cell type OCRs between mouse and human profiles as
481 well as shared enrichments between traits **(Figure 5B)**. Genetic variants associated with both
482 `SmokingInitiation` and `Cannabis` enriched in mouse-human orthologous OCRs of
483 cortical EXC **(Figure 3B)**, concordant with enrichments in human cortical NeuN+ OCRs
484 **(Figure 1B)**, which were predicted to include EXC neurons **(Figure 4B)**. Genetic variants from
485 these two traits showed replicable enrichment in human EXC neuron OCRs of **isocortex and**
486 occipital cortex **(Figure 1C-D**), providing strong evidence that genetic variation in cortical
487 excitatory neuron OCRs confers susceptibility to nicotine and cannabis use behaviors. **The**
488 **enrichments of genetic variants associated with `Cannabis` in isocortical IN neuron OCRs**
489 **(Figure 1C) and mouse-human orthologous OCRs of cortical PV neurons (Figure 3B)**
490 **suggest that genetic variation in cortical PV neuron OCRs also confer susceptibility of**
491 **cannabis use behavior.** Within striatal regions, D1 and D2 MSN mouse-human orthologous
492 OCRs enriched for genetic variants of all measured addiction-associated traits **(Figure 2B)**, with
493 strongest concordance in human OCRs for genetic variants associated with
494 `SmokingCessation` and `DrinksPerWeek` **(Figure 3B, Figure 5B)**. The enrichments in
495 conserved OCRs of MSN subtypes in the dorsal striatum and nucleus accumbens unsurprisingly
496 emphasize known roles of MSNs of both areas to drive and maintain addiction behaviors
497 (Ferguson et al., 2011; Ji et al., 2017). **Our validations of enrichments both at the tissue and**
498 **cell type level across human and human-orthologous OCRs agree with LDSC regression**
499 **GWAS enrichments of non-coding regions around differentially expressed genes in DLPFC**

500 **and NAc measured from postmortem human subjects who were diagnosed with opioid use**
501 **disorder vs. neuropsychiatric controls** (Seney et al., 2020)**. Due to the conservation of**
502 **reward circuit between mouse and human, our approach is able to unravel the cell types in**
503 **which genetic variation at the epigenome level predisposes addiction-related traits even**
504 **from measurements in organisms that have not been exposed to addictive substances.**
505 **Further, this level of OCR conservation is present at the level of excitatory cell types in**
506 **cortical brain regions (cite). This may explain why we found enriched cell types in occipital**
507 **cortex (Figure 1D), which is not well-defined for its role in addiction-related traits.**
508 In an orthogonal approach to mapping mouse-human orthologous OCRs, **we devised and**
509 **trained convolutional neural network (CNN) models to classify the neuronal subtype**
510 **membership of mouse and human NeuN+ OCRs in order to refine GWAS enrichments of**
511 **bulk tissue to the major neuronal subtypes of cortex and striatum. This approach can**
512 **provide further validation for enrichments of human and mouse-human orthologous OCRs**
513 **in cell types and tissues.** Refinement of NeuN+ OCRs revealed that addiction-associated traits
514 enriched for two clusters of cell types and brain regions. The first group, which displays
515 concordant cortical excitatory enrichments between human and mouse, consists of
516 `SmokingInitiation` and `Cannabis` **(Figure 3B)**, and the second group, which displays
517 concordant D1 and D2 MSN enrichments, consists of `SmokingCessation` and
518 `DrinksPerWeek`. A draw-back of assigning human NeuN+ OCR membership to individual
519 cell types lies in the considerably low representation of interneurons in both cortical and striatal
520 neuron populations - as low as 12% in neocortex (Beaulieu, 1993; Lefort et al., 2009) and ~5%
521 in striatum (Tepper and Koós, 2017; Krienen et al., 2019). NeuN+ open chromatin profiles alone
522 do not always capture OCRs unique to rare interneurons, some of which had OCRs identified by

523 human single-cell assays and mouse-human orthologs enriched for addiction GWAS variants
524 **(Figure 1C, Figure 2B)**. As a result, we did not train **CNN** models for PV, SST, or VIP
525 interneurons. However, the striking enrichments of OCRs from certain interneuron populations
526 for addiction GWAS variants begin to demonstrate these populations' roles in the addiction
527 neural circuits (Bracci et al., 2002; Lansink et al., 2010; Wiltschko et al., 2010; Ribeiro et al.,
528 2018; Jiang et al., 2019; Lee et al., 2020; Schall et al., 2020).

529 The overall concordance of enrichments across human and mouse-human orthologous
530 OCRs suggests a conserved regulatory **code** between mouse and human CREs. Correspondence
531 in the neural circuitry has been well-appreciated between human studies and rodent models of
532 addiction (Berke and Hyman, 2000; Koob and Volkow, 2016; Farrell et al., 2018), and our study
533 further demonstrates that mouse-human conserved OCRs may explain considerable heritability
534 of addiction-associated traits. This makes animal models suitable not only for studying the neural
535 circuits of addiction but also cell-type-specific gene-regulatory mechanisms of addiction.

536 We used several selection criteria along with **CNN** models to predict the functional
537 impact of genetic variants **associated with** addiction-**related** traits **(Figure 5, Supplemental**
538 **Figure 5, Supplemental Table 1)**. The fine-mapping pipeline described effectively narrows
539 down a set of 14,790 SNPs to a putatively functional set of **55 Tier A candidate causal SNPs**
540 that can be experimentally tested to determine which brain regions and neuronal subtypes they
541 would have function in. The candidate functional SNPs that our models prioritize demonstrate
542 how a candidate SNP within a locus, such as rs7604640 **(Figure 4B)**, might act in **distinct**
543 neuronal subtypes and brain regions. **Cell type-and brain region-specificity adds complexity**
544 **to identifying how genetic variation may alter gene regulation to predispose individual to**
545 **addiction-associated traits. Our approach often reported one to four candidates per loci,**

546 **even in stretches of SNPs in perfect LD such as the MAPT-CRHR1 locus (Supplemental**
547 **Figure 5D)**. This reflects the idea that many SNPs in the same loci are significantly associated
548 with addiction due to LD with **only one or a few** causal SNPs and **are unlikely to** influence
549 addiction-associated genetic predisposition. **We report many** candidate SNPs that **also** overlap
550 mouse-human orthologs from the same predicted cell type raise the idea that altering the
551 conserved regulatory DNA sequence may be a mechanism of cell type-specific gene regulatory
552 tuning in a population or even across species (Gjoneska et al., 2015).

553 Our study depends solely on assays of open chromatin as a proxy for putative CREs.
554 Epigenetic assays for chromatin conformation, histone modifications, and methylation would
555 further inform how putative CREs regulate nearby gene expression. While eQTL studies do not
556 control for inflated associations due to LD and report gene expression differences from bulk
557 tissue, we do note that our approach prioritizes several SNPs known to be *cis*-eQTLs in relevant
558 brain regions, which indirectly affirms our framework's ability to select SNPs with functional
559 impacts on gene regulation. **Although *cis*-EQTLs are often not cell type- or tissue-specific,**
560 **our findings of risk loci in brain regions implicated in addiction-related traits reflect a**
561 **strength of our approach in discerning brain-specific signal.** In order to validate our
562 predictions, it will be necessary to further investigate candidate genetic variants such as
563 rs7604640 **(Figure 4B)** in future studies using **a fluorescence reporter assay or *in situ***
564 **hybridization studies. These methods can measure regulatory activity differences between**
565 **risk and non-risk alleles to verify our predictions of SNP impact on putative CREs and**
566 **indicate whether the reported differences in regulatory activity are cell type-specific.** The
567 candidate SNPs we identified provide possible mechanisms linking differences in genetic make-

568 up with the genes, cell types, and brain regions that could influence addiction and substance use

569 behaviors **(Figure 4)**.

570 **MATERIALS & METHODS**

571 **ATAC-seq data processing pipeline:**

572 We processed raw FASTQ files of ATAC-seq experiments with the official ENCODE ATAC-
573 seq pipeline (Landt et al., 2012) accessed by https://github.com/ENCODE-DCC/atac-
574 seq-pipeline. We ran this pipeline using the mm10 genome assembly for mouse and the
575 hg38 genome for human with the following settings: smooth_win = 150, multimapping
576 = 0, idr_thresh = 0.1, cap_num_peak = 300,000,
577 keep_irregular_chr_in_bfilt_peak = true. We grouped biological replicates
578 when processing data to obtain individual de-duplicated, filtered bam files and reproducible
579 (IDR) peaks for each condition. Unless otherwise stated, we used the optimal reproducible set of
580 peaks for downstream analyses. We removed samples that had low periodicity indicated by
581 ENCODE quality control metrics and reprocessed the remaining replicates with the pipeline.

582 **Publicly available datasets**

583 Fullard *et al.* NeuN-sorted ATAC-seq of human postmortem brain (Fullard et al., 2018): We
584 identified OCRs overlapping addiction-related variants through analysis of human postmortem
585 brain ATAC-seq in which cells were sorted into NeuN-positive and NeuN-negative groups via
586 fluorescence activated nuclei sorting (FANS); the brain regions we used were dorsolateral
587 prefrontal cortex (DLPFC), orbitofrontal cortex (OFC), ventrolateral prefrontal cortex (VLPFC),
588 anterior cingulate cortex (ACC), superior temporal gyrus (STC), inferior temporal gyrus (ITC),
589 primary motor cortex (PMC), insula (INS), primary visual cortex (PVC), amygdala (AMY),
590 hippocampus (HIP), mediodorsal thalamus (MDT), nucleus accumbens (NAc), and putamen
591 (PUT). We downloaded data from the Sequence Read Archive (SRA) through Gene Expression
592 Omnibus (GEO) accession #GSE96949. We separated samples by cell type and reprocessed

593 them with the ENCODE pipeline as detailed above, aligning reads to `hg38`. We used the
594 "optimal reproducible peaks" for each cell type and brain region as foregrounds in GWAS LDSC
595 enrichment with the Honeybadger2 OCR set as the background set (see LDSC Regression
596 GWAS Enrichment Backgrounds).

597 **Corces *et al*. human isocortex, striatum, hippocampus, and substantia nigra single cell**
598 **chromatin accessibility profiling** (Corces et al., 2020)**: We downloaded 24 clusters of IDR**
599 **peaks in BED format through GEO accession #GSE147672. These clusters represent cell**
600 **populations defined by Corces *et al* from the measured brain regions. We assigned clusters**
601 **to cell populations as described in Corces *et al*: astrocyte (clusters 13, 17), hippocampal**
602 **excitatory (clusters 3-4), isocortical astrocyte (cluster 15), isocortical excitatory (cluster 1),**
603 **isocortical inhibitory (cluster 11), microglia (cluster 24), neuron (cluster 7), nigral astrocyte**
604 **(cluster 14), nigral neurons (clusters 5-6), nigral oligodendrocyte precursor (cluster 10),**
605 **oligodendrocyte (clusters 19-23), oligodendrocyte precursor (clusters 8-9), striatal astrocyte**
606 **(cluster 16), and striatal inhibitory cells (clusters 2, 12). We did not include cluster 18,**
607 **which corresponds to a doublet. We merged coordinates from clusters assigned to the same**
608 **cell types to define foreground sets for LDSC regression GWAS enrichment. We merged**
609 **the foreground sets with the Honeybadger2 OCR set to define the background set (LDSC**
610 **regression GWAS Enrichment Backgrounds).**

611 Lake *et al.* human occipital cortex scTHS-seq (Lake et al., 2018): We downloaded BED-
612 formatted cell type-specific differential OCRs from occipital cortex scTHS-seq of excitatory
613 neurons (EXC), inhibitory neurons (IN), astrocytes (AST), endothelial cells (END),
614 oligodendrocyte precursor cells (OPC), oligodendrocytes (OLI), and microglia (MIC) from the
615 GEO subseries #GSE97887. We used the `hg38` OCR coordinates as foregrounds in LDSC

616 regression GWAS enrichment with the Honeybadger2 OCR set as the background set (LDSC
617 regression GWAS Enrichment Backgrounds).
618 Mo *et al.* mouse INTACT-sorted nuclei ATAC-seq (Mo et al., 2015): We downloaded FASTQ
619 files of *R26-CAG-LSL-Sun1-sfGFP-Myc* transgenic mouse lines for cell type-specific ATAC-seq
620 performed using the INTACT method from the accession #GSE63137. *Mo et al.* isolated
621 INTACT-enriched nuclei from three cell types: excitatory neurons (EXC, *Camk2a-cre*),
622 vasoactive intestinal peptide neurons (VIP, *Vip-cre*), and parvalbumin neurons (PV, *Pvalb-cre*).
623 We reprocessed the data with the Kundaje Lab open chromatin pipeline using the mm10 genome
624 (`https://github.com/kundajelab/atac_dnase_pipelines`). We mapped
625 reproducible mouse ATAC-seq peaks for each cell type to `hg38` using halLiftover with the 12-
626 mammals Cactus alignment (Paten et al., 2011; Hickey et al., 2013) followed by HALPER
627 (Zhang et al., 2020) (Mapping mouse OCR orthologs) to produce a foreground set of orthologous
628 human sequences for LDSC regression GWAS enrichment (Finucane et al., 2018). We mapped
629 the ENCODE `mm10` DNaseI-hypersensitive peak set (Yue et al., 2014) to `hg38` (Mapping
630 mouse OCR orthologs) and used successfully mapped hg38 orthologs of mm10 OCRs a
631 background set for mouse foreground enrichments. Furthermore, we used this dataset to evaluate
632 differential accessibility in cSNAIL-INTACT PV and PV-negative ATAC-seq samples and
633 develop **convolutional neural network** models of cell type-specific open chromatin (see
634 Methods below).
635 Human negative control foregrounds (ENCODE Project Consortium, 2012; Thurman et al.,
636 2012; Davis et al., 2018; Cannon et al., 2019): We downloaded raw ATAC-seq profiles of
637 human adult female and male stomach ATAC-seq generated by Snyder *et al*. (ENCSR337UIU,
638 ENCSR851SBY, respectively), female human embryonic liver DNase-seq generated by

639 Stamatoyannopoulos *et al*. (ENCSR562FNN), and human embryonic lung DNase-seq generated
640 by Stamatoyannopoulos *et al*. (ENCSR582IPV) from
641 `https://www.encodeproject.org/`. We processed these files using the ENCODE
642 pipeline as detailed above to obtain optimal reproducible `hg38` peaks. We also downloaded
643 BED files of human adipocyte and preadipocyte ATAC-seq profiles generated by Cannon *et al*.
644 from GEO accession number #GSE110734. We mapped these BED coordinates from `hg19` to
645 `hg38` using liftOver to define negative control foregrounds for human LDSC regression GWAS
646 enrichment. We merged the human negative control foregrounds and Fullard *et al.* foregrounds
647 with the Honeybadger2 OCR set to define the background for human negative control
648 foreground enrichments.
649 Human-orthologous negative control foregrounds (Liu et al., 2019a): We also downloaded raw
650 ATAC-seq data profiled in female mouse kidney, female mouse liver, and male mouse lung
651 generated by Liu *et al.* from SRA accession #SRP167062 to define human-orthologous negative
652 control foregrounds. We processed these files using the ENCODE pipeline as detailed above to
653 get optimal reproducible peaks. We mapped optimal reproducible peaks from `mm10` to `hg38`
654 using halLiftover with the 12-mammals Cactus alignment followed by HALPER (Mapping
655 mouse OCR orthologs) to define negative control foregrounds for human-orthologous LDSC
656 GWAS enrichments. We merged all human orthologous foregrounds with the human orthologs
657 of the ENCODE `mm10` DNaseI-hypersensitive peak set to define a background for human-
658 orthologous LDSC GWAS enrichments.
659 **<u>Mapping mouse open chromatin region (OCR) orthologs</u>**
660 We employed halLiftover (Hickey et al., 2013) with the 12-mammals Cactus alignment (Paten et
661 al., 2011) followed by HALPER

662 (https://github.com/pfenninglab/halLiftover-postprocessing) (Zhang et
663 al., 2020) to map mm10 mouse reproducible OCRs to hg38 human orthologs in order to perform
664 LDSC regression GWAS enrichment. The Cactus multiple sequence alignment file (Paten et al.,
665 2011) has 12 genomes, including mm10 and hg38, aligned in a reference-free manner, allowing
666 us to leverage multi-species alignments to confidently identify orthologous regions across
667 species. halLiftover uses a Cactus-format multiple species alignment to map BED coordinates
668 from a query species to orthologous coordinates of a target species, and HALPER constructs
669 contiguous orthologs from the outputs of halLiftover (Zhang et al., 2020). We ran the
670 orthologFind.py function from HALPER on the outputs of halLiftover using the following
671 parameters: -max_frac 5.0 -min_frac 0.05 -protect_dist 5 -narrowPeak
672 -mult_keepone. In general, 70% of mouse brain ATAC-seq reproducible peaks were able to
673 be mapped to confident human orthologs. To map the ENCODE mm10 mouse DHS background,
674 which does not contain summit information, to hg38 we used the mouse coordinates of position
675 with the most species aligned in a region to define the summit. Only for the mm10 mouse DHS
676 background set, for which a significant proportion of regions could not be confidently mapped to
677 hg38, we flanked the original assembly coordinates by 300 bp to increase OCR mapping from
678 54% to 64%.

679 **LDSC Regression GWAS Enrichment Backgrounds:**

680 We found that LDSC regression GWAS enrichment analysis is sensitive to the selected
681 background set of matched regions. To construct appropriate background sets for each GWAS
682 enrichment, we used the ENCODE and RoadMap Honeybadger2(Roadmap Epigenomics
683 Consortium et al., 2015) and Mouse DHS peak sets for the respective human and mouse-based
684 open chromatin GWAS enrichment. The Honeybadger2 set, downloaded from

685 https://personal.broadinstitute.org/meuleman/reg2map/, consists of
686 DNaseI-hypersensitive OCRs across 53 epigenomes consisting of promoter, enhancer, and
687 dyadic regions. Honeybadger2 is an appropriate epigenetic reference for enrichment of cell type-
688 specific open chromatin from various foregrounds such as the Fullard *et al.* and Lake *et al*.
689 Honeybadger2 regions allow the LDSC algorithm to properly account for the heritability from
690 OCRs of a particular cell type or regions rather than because they tend to be more conserved, are
691 enriched for ubiquitously active transcription factor motifs, or other factors distinguishing open
692 chromatin from heterochromatin. The human orthologs of the ENCODE Mouse DHS peak set,
693 downloaded through the ENCODE ATAC-seq pipeline at
694 http://mitra.stanford.edu/kundaje/genome_data/mm10/ataqc/mm10_un
695 iv_dhs_ucsc.bed.gz, is a set of peaks combined from mouse DNaseI-hypersensitivity
696 OCRs from ENCODE and provides a background for human orthologs of mouse OCRs. The
697 mm10 mouse DHS regions were mapped to hg38 as described in **Mapping mouse OCR**
698 **orthologs**. For each respective foreground-background pairing, the foreground regions were
699 merged with the background reference to ensure the background always contained the
700 foreground set. The mouse background was used to calculate the significance of the relationship
701 between mouse OCRs and GWAS for addiction-associated traits to control for a possible
702 association between the degree to which a region is conserved and its likelihood in influencing
703 the predisposition to an addiction-associated trait.

704 **GWAS enrichment with partitioned LD score regression analysis**

705 We computed the partitioned heritability of CREs for GWAS variants using the LDSC
706 regression pipeline for cell type-specific enrichment as outlined in
707 https://github.com/bulik/ldsc/wiki/Cell-type-specific-analyses

708 (Bulik-Sullivan et al., 2015b). We downloaded the GWAS summary statistics files and processed
709 them with the LDSC `munge_sumstats` function to filter rare or poorly imputed SNPs with
710 default parameters. We munged the summary statistics files for HapMap3 SNPs excluding the
711 MHC regions downloaded at
712 `http://ldsc.broadinstitute.org/static/media/w_hm3.noMHC.snplist.`
713 `zip`. We inspected GWAS file to ensure the effect allele, non-effect allele, sample size, p-value,
714 and signed summary statistic for each SNP in each GWAS were included and appropriate for
715 LDSC. The addiction-associated GWAS measure genetic predisposition for age of smoking
716 initiation (`AgeofInitiation`) (Liu et al., 2019b), heaviness of smoking
717 (`CigarettesPerDay`) (Liu et al., 2019b), having ever regularly smoked
718 (`SmokingInitiation`) (Liu et al., 2019b), current versus former smokers
719 (`SmokingCessation`) (Liu et al., 2019b) , alcoholic drinks per week (`DrinksPerWeek`)
720 (Liu et al., 2019b), cannabis consumption (`Cannabis`) (Pasman et al., 2018), and risk tolerance
721 (`RiskyBehavior`) (Karlsson Linnér et al., 2019). GWAS traits related to addiction include
722 multisite chronic pain (`ChronicPain`) (Johnston et al., 2019) and number of coffee cups drank
723 per data (`CoffeePerDay`) (Coffee and Caffeine Genetics Consortium et al., 2015). Other
724 addiction-related traits come from underpowered GWAS including opioid dependence
725 (`OpioidDep`) (Cheng et al., 2018) , cocaine dependence (`CocaineDep`) (Cabana-Domínguez
726 et al., 2019), and diagnosis of obsessive-compulsive disorder (`OCD`) (International Obsessive
727 Compulsive Disorder Foundation Genetics Collaborative (IOCDF-GC) and OCD Collaborative
728 Genetics Association Studies (OCGAS), 2018). GWAS from strong brain-related traits used are
729 schizophrenia risk (Schizophrenia)(Schizophrenia Working Group of the Psychiatric Genomics
730 Consortium, 2014), highest level of educational attainment (`EduAttain`) (Lee et al., 2018), and

731 sleep duration (SleepDuration) (Dashti et al., 2019). The non-brain related traits measure
732 genetic liability for lean body mass (LBM) (Zillikens et al., 2017), bone mineral density (BMD)
733 (Kemp et al., 2017), and coronary artery disease (CAD) (Howson et al., 2017).

734 We estimated LD scores for each foreground set and corresponding background set with
735 the LDSC regression pipeline make_annot and ldsc functions using hg38 1000 Genomes
736 European Phase 3 European super-population (1000G EUR) cohort plink files downloaded from
737 https://data.broadinstitute.org/alkesgroup/LDSCORE/GRCh38/. An
738 example of an ATAC-seq optimal set of reproducible peaks mapped to hg38 in narrowPeak
739 format is annotated with 1000G EUR LD scores using the following call:

```
740 python make_annot.py \
741 --bed-file optimal_peak.narrowPeak.gz \
742 --bimfile 1000G.EUR.hg38.${chr}.bim \
743 --annot-file foreground.${chr}.annot
```

744 We downloaded the baseline v1.2 files for cell type-specific enrichment in hg38
745 coordinates from the same link above as well as the corresponding weights
746 `weights.hm3_noMHC' file excluding the MHC region from
747 https://data.broadinstitute.org/alkesgroup/LDSCORE/. HapMap SNPs
748 and corresponding weights file used in the LDSC analyses only refer to the SNP rsIDs, rather
749 than genomic coordinates, so only the baseline and LD statistics used to annotate the foreground
750 and background files must be in hg38 coordinates. In accordance with the LDSC regression
751 script input format, we created an `enrichment.ldcts' file listing the annotated
752 foreground/background pair for each foreground set. We estimated the partitioned heritability
753 using the ldsc function, which integrates the foreground and background LD score estimates,

754 munged GWAS SNP data, baseline variant data, and variants weights. The final function call to
755 GWAS enrichment is as follows:

```
756 python ldsc.py --h2-cts $Munged_GWAS \
757        --ref-ld-chr baseline_v1.2/baseline. \
758        --w-ld-chr weights.hm3_noMHC. \
759        --ref-ld-chr-cts enrichment.ldcts \
760        --out $Output_Label
```

761 The pipeline produced LD score regression coefficient, coefficient error, and coefficient
762 p-value estimates. We adjusted for multiple testing using the false discovery rate on p-values of
763 the LD score regression coefficients (`alpha = 0.05`) on all 18 GWAS traits intersected on
764 within the same foreground/background set. A significant FDR-value indicates enrichment of the
765 foreground genomic regions for GWAS SNPs relative to the background. Lastly, we computed
766 genetic correlations in **Supplemental Figure 1A** between GWAS of addiction-associated traits
767 using the pre-munged summary statistics as described by Bulik-Sullivan *et al.* (Bulik-Sullivan et
768 al., 2015a)

769 **<u>Bulk tissue ATAC-seq</u>**

770 To augment and compare to mouse cell type-specific ATAC-seq datasets generated in this study,
771 we also performed bulk tissue ATAC-seq from cortex (CTX) and dorsal striatum/nucleus
772 accumbens (CPU) of 7- and 12-week-old C57Bl/6J mice (N = 2 each age) as described in
773 Buenrostro *et al.*, 2015(Buenrostro et al., 2015) with the following minor differences in buffers
774 and reagents. We euthanized mice with isoflurane, rapidly decapitated to extract the brain, and
775 sectioned it in ice-cold oxygenated aCSF (119mM NaCl, 2.5 mM KCl, 1mM
776 NaH_2PO_4(monobasic), 26.2mM $NaHCO_3$, 11mM glucose) at 200-micron sections on a
777 vibratome (Leica VT1200). We further micro-dissected sections for cortex and dorsal striatum

778 on a stereo microscope and transferred dissected regions into chilled lysis buffer (Buenrostro et
779 al., 2015). We dounce homogenized the dissected brains in 5mL of lysis buffer with the loose
780 pestle (pestle A) in a 15mL glass dounce homogenizer (Pyrex #7722-15). We washed nuclei
781 lysate off the pestle with 5mL of lysis buffer and filtered the nuclei through a 70-micron cell
782 strainer into a 50mL conical tube. We washed the dounce homogenizer again with 10mL of BL
783 buffer and transferred the lysate through the 70-micron filter (Foxx 1170C02). We pelleted the
784 20 mL of nuclei lysate at 2,000 x *g* for 10 minutes in a refrigerated centrifuge at 4°C. We
785 discarded the supernatant and resuspended the nuclei in 100-300 microliters of water to
786 approximate a concentration of 1-2 million nuclei/ mL. We filtered the nuclei suspension through
787 a 40-micron cell strainer. We stained a sample of nuclei with DAPI (Invitrogen #D1206) and
788 counted the sample to measure 50k nuclei per ATAC-seq transposition reaction. The remaining
789 steps follow the Buenrostro *et al.*, 2015 (Buenrostro et al., 2015) protocol for tagmentation and
790 library amplification. We shallowly sequenced barcoded ATAC-seq libraries at 1-5 million reads
791 per sample on an Illumina MiSeq and processed individual samples through the ENCODE
792 pipeline for initial quality control. We used these QC measures (clear periodicity, library
793 complexity, and minimal bottlenecking) to filter out low-quality samples and re-pooled a
794 balanced library for paired-end deep sequencing on an Illumina NextSeq to target 30 million
795 uniquely mapped fragments per sample after mitochondrial DNA and PCR duplicate removal.
796 These raw sequencing files entered processing through the ENCODE ATAC-seq pipeline as
797 above by merging technical replicates and grouping biological replicates by brain region for each
798 pipeline run.

799 **Cre-Specific Nuclear-Anchored Independent Labeling (cSNAIL) virus procedures**

800 The cSNAIL genome (pAAV-Ef1a-DIO-Sun1-Gfp-WPRE-pA) contains *loxP* sites to invert the
801 *Sun1-Gfp* fusion gene and integrate into the nuclear membrane of cells expressing the *Cre* gene,
802 allowing these cell populations to be profiled for various genomic assays (Lawler et al, 2020 in
803 press J. Neuro). We packaged the cSNAIL genome with AAV variant PHP.eB (pUCmini-iCAP-
804 PHP.eB) in AAVpro(R) 293T cells (Takara, cat #632273). Viviana Gradinaru provided us with
805 the pUCmini-iCAP-PHP.eB (http://n2t.net/addgene:103005; RRID: Addgene 103005) (Chan et
806 al., 2017). We precipitated viral particles with polyethylene glycol, isolated with
807 ultracentrifugation on an iodixanol density gradient, and purified in PBS with centrifugation
808 washes and 0.2μM syringe filtration. We injected each mouse with 4.0 x 10^{11}vg into the retro-
809 orbital cavity under isoflurane anesthesia. We allowed the virus to incubate in the animal for 3-4
810 weeks to reach peak expression. We closely monitored the health of the animals throughout the
811 length of the virus incubation and did not note any concerns.

812 **cSNAIL nuclei isolation**

813 On the day of the ATAC-seq experiments, we dissected brain regions from fresh tissue and
814 extracted nuclei in the same manner as described for bulk tissue experiments. Then, we sorted
815 the nuclei suspension into Sun1GFP+ (Cre+) and Sun1GFP- (Cre-) fractions using affinity
816 purification with Protein G Dynabeads (Thermo Fisher, cat. 10004D). A pre-clearing incubation
817 with beads and nuclei for 10-15 minutes removes effects from non-specific binding events. Next,
818 we incubated the remaining free nuclei with anti-GFP antibody (Invitrogen, #G10362) for 30
819 minutes to bind Sun1GFP. Finally, we added new beads to the solution to conjugate with the
820 antibody and incubated the reaction for an additional 20 minutes. The pre-clear step and all
821 incubations took place in wash buffer (0.25M Sucrose, 25mM KCl, 5mM $MgCl_2$, 20mM Tricine
822 with KOH to pH 7.8, and 0.4% IGEPAL) at 4°C with end-to-end rotation. After the binding

823 process, we separated bead-bound nuclei on a magnet, washed three times with wash buffer, and
824 filtered through a 20µM filter to ensure purity. We resuspended nuclei in nuclease-free water for
825 input into the ATAC-seq tagmentation reaction. We performed nuclei quantification and
826 tagmentation in the same manner described for bulk tissue ATAC-seq above. We list in the table
827 below the number of animals, the genotypes, and which regions collected for ATAC-seq
828 experiments in this study. N=2 *Pvalb-cre* samples from CPU/NAc region had received a sham
829 surgery with saline injection into the external globus pallidus 5 days before they were sacrificed.
830 **The background for all transgenic mice is C57BL/6J. SST-Cre mice were homozygous for**
831 **the transgene while PValb-2a-Cre, D1-Cre, and A2a-Cre mice were heterozygous for the**
832 **transgene (Lawler et al., 2020)**. N=2 *Drd1-cre* samples from both CPU and NAc regions had
833 received headcap surgeries 3 weeks before they were sacrificed. Both *Pvalb-cre* and *Drd1-cre*
834 were overall healthy at time of sacrifice.

Genotype	**Replicates**	**Sex** (**F**emale /**M**ale)	**Region and Replicate per region**	**Cell type**
C57BL/6 WT	N=4	2 F, 2 M	CTX= 4, CPU/NAc = 4	bulk
Pvalb-cre	N=5	3 F (CTX) 1 F, 1 M (CPU/NAc)	CTX= 3, CPU/NAc = 2	PV
Sst-cre	N=2	1 F, 1 M	CTX= 2, CPU/NAc = 2	SST
Drd1-cre	N=2	2 F	CPU=2, NAc=2	D1
Adora2a-cre	N=2	2 F	CPU=2, NAc=2	D2

835

836 **cSNAIL Cell Type Specificity**

837 We created a consensus set of non-overlapping IDR peaks from the ATAC-seq pipeline for
838 cSNAIL ATAC-seq and Mo *et al.* INTACT samples (`Tissue`: Ctx, CPU, and NAc ;
839 `Celltype`: EXC, PV, SST, VIP, D1, D2). We extended the peak set 200bp up- and down-
840 stream, count overlapping fragments with `Rsubread v2.0.1` using the de-duplicated BAM
841 files from the pipeline(Liao et al., 2014), and created with `DESeq2 v1.26.0` a variance-

842 stabilized count matrix aware of experimental `Group` (combination of `Tissue` and
843 `Celltype`) with `~Group` (Love et al., 2014). We plotted the principle component analysis in
844 **Supplemental Figure 3A** for the first two components with this variance-stabilized count
845 matrix. We used `Deeptools v3.5.0` to convert the same BAM files to normalized bigWig
846 files and average over replicates of the same `Group` (Ramírez et al., 2016). We plotted the
847 tracks using `pyGenomeTracks v3.5` around marker genes for each cell type (*Slc17a7*, *Drd1*,
848 *Adora2a*, *Pvalb*, *Sst*, *Vip*) (Ramírez et al., 2018) **Supplemental Figure 3B**. We computed the
849 mean accessibility for each `Group` 2kb up- and down-stream the transcription start sites (TSS)
850 and correlated $\log_{10}$ (TSS accessibility + 1) with gene expression $\log_{10}$(meta gene counts + 1) of
851 Drop-Seq annotated cell types from prefrontal cortex and striatum(Saunders et al., 2018). We
852 used the Saunders *et al.* tissue subcluster metagene profiles (sum of gene expression in all cells)
853 and summed subclusters to cluster-level metagene profiles. Most tissue cluster metagene profiles
854 corresponded to cSNAIL ATAC-seq celltype and tissue profiles, with the exception of cSNAIL
855 cortical PV+ samples were matched to Saunders *et al.* cortical MGE+ interneuron clusters.
856

857 **Convolutional Neural Network models for CRE cell type classification**

858 We trained a set of convolutional neural network (CNN) models to learn the regulatory **code** of a
859 given cell type from the DNA sequences underlying the cell type's OCRs. The models take in
860 one-hot encoded 501bp genomic sequences **to predict 1 for an OCR or 0 for non-OCR**
861 **sequence**. Positive sequences were centered on IDR peak summits that are annotated to be in
862 introns and distal intergenic regions and negative sequences are approximately ten times the
863 number of positives sequences that are G/C-matched and not overlapping IDR peaks. We
864 excluded promoters (defined as within 5,000bp from the TSS) and exons because distal

865 sequences have been shown to confer more cell type-specificity and be more predictive of
866 expression levels of regulated genes (Roadmap Epigenomics Consortium et al., 2015). We
867 constructed the negative set by first building a sequence repository `$BGDIR` according to
868 https://bitbucket.org/CBGR/biasaway_background_construction/src/
869 master/ from the mouse `mm10` genome using 501bp sequences. Then we used the `biasaway`
870 (Worsley Hunt et al., 2014; Khan et al., 2020) command-line interface to generate negative
871 sequences with the matching nucleotide distribution along a sliding window of the 501bp IDR
872 peak sequence:

```
biasaway c --foreground $FGFASTA --nfold 10 --deviation 2.6 --
step 50 --seed 1 -winlen 100 --bgdirectory $BGDIR
```

875 We employed a 5-fold cross validation chromosome hold-out scheme to train 5 models per set of
876 IDR peaks to ensure stable and consistently learned regulatory patterns. A model that was
877 training a fold did not see sequences during training from the validation set for that fold, and no
878 model saw the test set until final model performance evaluation. Sequences from these
879 chromosomes were used as the validation set for each fold:

880 fold1: {`chr6, chr13, chr21`}
881 fold2: {`chr7, chr14, chr18`}
882 fold3: {`chr11, chr17, chrX`}
883 fold4: {`chr9, chr12`}
884 fold5: {`chr10, chr8`}.

885 We used sequences from chromosomes {`chr1, ch2, chr19`} for the test set.

886 We trained the models with Keras `v2.3.0-tf` (https://keras.io/) implemented
887 through Tensorflow `v2.2.0` and used stochastic gradient descent (SGD) with Nesterov

888 momentum to minimize the binary cross entropy loss and learn model parameters. All models
889 used the same CNN **architecture after a grid-search of hyperparameters found stable and**
890 **high validation performance by area under the precision-recall curve (auPRC) in an**
891 **architecture with five Conv1D layers (`kernel_size = 11, filters = 200,`**
892 **`activation= 'relu', kernel_regularizer=l2(1e-10)`) sandwiched between**
893 **four Dropout layers (`rate = 0.25`), then one MaxPooling1D layer (`pool_size =`**
894 **`26, strides = 26`), one Flatten layer, one Dense layer (`units = 300,`**
895 **`activation=`relu`, kernel_regularizer=l2(1e-10)`), one Dropout layer**
896 **(`rate = 0.25`), a final output Dense layer (`units=1, activation = 'sigmoid',`**
897 **`kernel_regularizer=l2(1e-10)`), and a final Dropout layer (`rate = 0.25`) before**
898 **the sigmoid output layer**. We applied the One-Cycle-Policy (OCP) with linear cyclical learning
899 rate and momentum between a base and max rates as described previously (Smith, 2018) to train
900 each fold with `batch_size=` **`1000`**, `epochs = 23`, `num_cycles = 2.35`,
901 `base_learning_rate = 1e-2`, `max_learning_rate = 1e-1`, `base_momentum`
902 `= .85`, `max_momentum = 0.99`. **With these hyperparameters, we** trained models across
903 folds to predict positive OCRs of all **measured** cell types against an approximately 1:10
904 positive:negative class **ratio**. We computed classifier performance metrics including weighted
905 accuracy (using threshold = 0.5), weighted f1_score (using threshold = 0.5), area under receiver
906 operating characteristic (auROC), and area under precision-recall curve (auPRC). **Given the**
907 **class imbalance, we selected the reported hyperparameters that maximize the validation**
908 **auPRC at a threshold of 0.5. We report the test performance auPRC, F1 score, and false**
909 **positive rate on 10X nucleotide-content matched negatives in Supplemental Figure 5A. We**

910 **provide both the scripts and trained Keras models at**
911 https://github.com/pfenninglab/addiction_gwas_enrichment.
912
913 **Interpretation of Convolutional Neural Network models**
914 **To ensure that the classification task decisions relied on biological sequence signatures and**
915 **not artifacts, we performed model interpretation using Deep SHAP `v0.37.0`** (Štrumbelj
916 and Kononenko, 2014; Shrikumar et al., 2017) **and TF-MoDISco** (Shrikumar et al., 2018)**. For**
917 **a random subsample of 2,000 true positive sequences from the validation set, we generated**
918 **per base importance scores and hypothetical importance scores relative to a reference set**
919 **of 500 true negative sequences from the validation set. These scores describe the**
920 **contribution of each base toward a positive model classification, which is a predicted OCR**
921 **in the given cell type. TF-MoDISco is an importance score-aware method that clusters**
922 **commonly important subsequences, called "seqlets", to define the learned motifs of the**
923 **model. We ran TF-MoDISco `v0.4.2.3` with the options `sliding_window_size=11,`**
924 **`flank_size=3, min_seqlets_per_task=3000, trim_to_window_size=11,`**
925 **`initial_flank_to_add=3, final_flank_to_add=3, kmer_len=7,`**
926 **`num_gaps=1,` and `num_mismatches=1`. The resulting motifs were filtered to remove**
927 **rare patterns with fewer than 100 supporting seqlets. Then, the motifs were visualized and**
928 **associated with known motifs using Tomtom** (Gupta et al., 2007) **version 5.3.3 with the**
929 **HOCOMOCO v11 FULL database and default parameters (Supplementary Table 2)**.
930
931 **Machine learning cell type-specific prioritization of *Fullard et al.* NeuN+ ATAC-seq peaks**

932 We used CNN model scores to classify whether a peak from *Fullard et al.* NeuN+ open
933 chromatin data is active in a neuronal subtype {EXC, D1, D2}. We took NeuN+ IDR
934 "optimal peaks" from regions significantly enriched for addiction-associated traits {OFC,
935 VLPFC, DLPFC, ACC, STC, PUT, NAc, **Figure 1A**}, extracted 501bp DNA sequences
936 of each centered on the summit, and scored each peak with cell type-specific machine learning
937 models trained with the appropriate tissue context (e.g., score cortical NeuN+ peaks with a
938 model trained with cortical EXC cell type). We averaged scores across model folds from the
939 same cell types and classified NeuN+ peaks with scores greater than 0.5 as active in that cell
940 type**, as this threshold was the most discriminative in classifying positive validation set**
941 **sequences (Supplemental Figure 5B)**. We defined these CNN-prioritized peaks as foregrounds
942 for LDSC regression GWAS enrichment analyses as described above. We created a consensus
943 set of peaks merging all model-prioritized peaks and the Honeybadger2 set of OCRs to be the
944 matched background, and we performed GWAS enrichment and computed FDR on all 18
945 GWAS traits (only enrichments for addiction-associated GWAS shown, **Figure 3**).
946

947 **Addiction-associated GWAS processing and cell type-specific candidate selection**

948 We collected the addiction-associated SNPs by submitting the summary statistics files for the
949 seven addiction-associated traits {AgeofInitiation (Liu et al., 2019b),
950 CigarettesPerDay (Liu et al., 2019b), SmokingInitiation (Liu et al., 2019b),
951 SmokingCessation (Liu et al., 2019b), DrinksPerWeek (Liu et al., 2019b), Cannabis
952 (Pasman et al., 2018), RiskyBehavior (Karlsson Linnér et al., 2019)} to the FUMA
953 webserver (Watanabe et al., 2017). FUMA computed LD R^2 based on the 1000 Genomes
954 European (1000G EUR) super-population reference (1000 Genomes Project Consortium et al.,

955 2015) via PLINK (Purcell et al., 2007), linked GWAS-significant lead SNPs to off-lead SNPs in
956 LD with the lead, and annotated functional consequences of genetic variants via ANNOVAR
957 based on ENSEMBL build 85 human gene annotations (Wang et al., 2010) **(Figure 1A)**.
958 ANNOVAR functional gene annotations for a SNP are as defined in the primary publication and
959 online: https://annovar.openbioinformatics.org/en/latest/user-
960 guide/gene/. **We scored all effect and non-effect alleles with each set of CNN models,**
961 **averaged predictions across folds, and calibrated CNN scores that predict activity using the**
962 **set of validation positive OCRs. We computed the ΔSNP probability effect by taking the**
963 **difference between the effect allele and the non-effect allele. Most SNPs reported by GWAS**
964 **are not expected to be the causal variant for a trait, so the distribution of ΔSNP probability**
965 **can be used to define a null distribution. We compute the p-value that an allele has a non-**
966 **zero ΔSNP probability by fitting a normal distribution of null ΔSNP probabilities. We**
967 **correct for multiple testing using the method swfdr `v1.12.0` to compute q-values to**
968 **control for a false-discoveries conditioned on potentially informative covariates (Boca and**
969 **Leek, 2018). Weighted FDR-correction methods, including swfdr, have been shown to be**
970 **robust to uninformative covariates and increase power to detect real differences for**
971 **informative covariates while controlling false discoveries (Korthauer et al., 2019). We**
972 **conditioned the proportion of expected null p-values on the following covariates**
973 **(Supplemental Figure 5E, step 4): the difference in GC content of the 501 surrounding the**
974 **SNP compared to the average GC content of positive sequences used to train each model**
975 **(GC content), the minor allele frequency (MAF) based on the European ancestry subjects**
976 **in the 1000G reference panel, whether the SNP overlapped a Fullard et al. NeuN+ OCR**
977 **(inNeuN peak), and whether a SNP was fine-mapped and predicted to be causal by**

978 **CAUSALdb using the European LD structure and an ensemble of statistical fine-mapping**
979 **tools (isCausal) (FINEMAP, CAVIARBF, PAINTOR) (Chen et al., 2015; Benner et al.,**
980 **2016; Kichaev et al., 2017; Wang et al., 2020). We applied an alpha of 0.05 on the false-**
981 **discovery q-values for all 14,790 SNPs scored across 5 sets of CNNs to determine**
982 **significantly large enough ΔSNP effects.**

983 To accompany cell type-specific activity predictions, we downloaded SNPs that are
984 reported *cis* expression quantitative trait loci (eQTL) in human cortex, frontal cortex (DLPFC),
985 anterior cingulate cortex (ACC), caudate, putamen, and the nucleus accumbens (NAc) from the
986 GTEX Consortium from `https://www.gtexportal.org/home/datasets(GTEx`
987 `Consortium, 2013, 2015)`. We identified genes for which at least one of the 170 SNPs is
988 an eQTL and plotted them as arcs in **Figure 4B** and **Supplemental Figure 4**. Locus plots are
989 generated with `pyGenomeTracks v3.5` tools (Ramírez et al., 2018).

990 For **Figure 4A**, we compared calibrated SNP probabilities of the either effect or non-
991 effect allele across each model and grouped them by whether they overlapped a cortical or
992 striatal NeuN+ OCR, NeuN- OCR, both, or neither, depending on whether the model was for
993 `EXC` or `D1/D2` neuronal subtypes, respectively. We computed 2-tailed t-tests between groups and
994 corrected for multiple comparisons with the family-wise Bonferroni method for N=18 tests from
995 three models and (4 choose 2) six possible comparisons per model. * $P < 0.05/N$, ** $P < 0.01/N$,
996 *** $P < 0.001/N$.

997

998 **DATA AVAILABILITY**

Code used to run intermediate and final analyses reported in this paper are available on the GitHub page: https://github.com/pfenninglab/addiction_gwas_enrichment. Sequencing output files for data generated in this study are deposited on the GEO at accession **GSE161374** (Reviewer access token: **`cropkwsgnnyxhgh`**). Questions and comments about data and analyses may be directed to the corresponding author.

1004 **Bibliography**

1005 1000 Genomes Project Consortium, Auton A, Brooks LD, Durbin RM, Garrison EP, Kang HM,
1006 Korbel JO, Marchini JL, McCarthy S, McVean GA, Abecasis GR (2015) A global
1007 reference for human genetic variation. Nature 526:68–74.
1008 Alipanahi B, Delong A, Weirauch MT, Frey BJ (2015) Predicting the sequence specificities of
1009 DNA- and RNA-binding proteins by deep learning. Nat Biotechnol 33:831–838.
1010 Barman P, Reddy D, Bhaumik SR (2019) Mechanisms of Antisense Transcription Initiation with
1011 Implications in Gene Expression, Genomic Integrity and Disease Pathogenesis. Non-
1012 coding RNA 5.
1013 Beaulieu C (1993) Numerical data on neocortical neurons in adult rat, with special reference to
1014 the GABA population. Brain Res 609:284–292.
1015 Benner C, Spencer CCA, Havulinna AS, Salomaa V, Ripatti S, Pirinen M (2016) FINEMAP:
1016 efficient variable selection using summary data from genome-wide association studies.
1017 Bioinformatics 32:1493–1501.
1018 Berke JD, Hyman SE (2000) Addiction, dopamine, and the molecular mechanisms of memory.
1019 Neuron 25:515–532.
1020 Boca SM, Leek JT (2018) A direct approach to estimating false discovery rates conditional on
1021 covariates. PeerJ 6:e6035.
1022 Bracci E, Centonze D, Bernardi G, Calabresi P (2002) Dopamine excites fast-spiking
1023 interneurons in the striatum. J Neurophysiol 87:2190–2194.
1024 Buenrostro JD, Giresi PG, Zaba LC, Chang HY, Greenleaf WJ (2013) Transposition of native
1025 chromatin for fast and sensitive epigenomic profiling of open chromatin, DNA-binding
1026 proteins and nucleosome position. Nat Methods 10:1213–1218.
1027 Buenrostro JD, Wu B, Chang HY, Greenleaf WJ (2015) ATAC-seq: A Method for Assaying
1028 Chromatin Accessibility Genome-Wide. Curr Protoc Mol Biol 109:21.29.1-21.29.9.
1029 Bulik-Sullivan B, Finucane HK, Anttila V, Gusev A, Day FR, Loh P-R, ReproGen Consortium,
1030 Psychiatric Genomics Consortium, Genetic Consortium for Anorexia Nervosa of the
1031 Wellcome Trust Case Control Consortium 3, Duncan L, Perry JRB, Patterson N,
1032 Robinson EB, Daly MJ, Price AL, Neale BM (2015a) An atlas of genetic correlations
1033 across human diseases and traits. Nat Genet 47:1236–1241.
1034 Bulik-Sullivan B, Loh P-R, Finucane HK, Ripke S, Yang J, Schizophrenia Working Group of the
1035 Psychiatric Genomics Consortium, Patterson N, Daly MJ, Price AL, Neale BM (2015b)
1036 LD Score regression distinguishes confounding from polygenicity in genome-wide
1037 association studies. Nat Genet 47:291–295.
1038 Bush WS, Moore JH (2012) Chapter 11: Genome-wide association studies. PLoS Comput Biol
1039 8:e1002822.
1040 Cabana-Domínguez J, Shivalikanjli A, Fernàndez-Castillo N, Cormand B (2019) Genome-wide
1041 association meta-analysis of cocaine dependence: Shared genetics with comorbid
1042 conditions. Prog Neuropsychopharmacol Biol Psychiatry 94:109667.
1043 Cannon ME, Currin KW, Young KL, Perrin HJ, Vadlamudi S, Safi A, Song L, Wu Y, Wabitsch
1044 M, Laakso M, Crawford GE, Mohlke KL (2019) Open Chromatin Profiling in Adipose
1045 Tissue Marks Genomic Regions with Functional Roles in Cardiometabolic Traits. G3
1046 (Bethesda) 9:2521–2533.
1047 Chan KY, Jang MJ, Yoo BB, Greenbaum A, Ravi N, Wu W-L, Sánchez-Guardado L, Lois C,
1048 Mazmanian SK, Deverman BE, Gradinaru V (2017) Engineered AAVs for efficient
1049 noninvasive gene delivery to the central and peripheral nervous systems. Nat Neurosci

1050 20:1172–1179.
1051 Chen L, Fish AE, Capra JA (2018) Prediction of gene regulatory enhancers across species
1052 reveals evolutionarily conserved sequence properties. PLoS Comput Biol 14:e1006484.
1053 Chen W, Larrabee BR, Ovsyannikova IG, Kennedy RB, Haralambieva IH, Poland GA, Schaid
1054 DJ (2015) Fine Mapping Causal Variants with an Approximate Bayesian Method Using
1055 Marginal Test Statistics. Genetics 200:719–736.
1056 Cheng Y, Huang CCY, Ma T, Wei X, Wang X, Lu J, Wang J (2017) Distinct synaptic
1057 strengthening of the striatal direct and indirect pathways drives alcohol consumption.
1058 Biol Psychiatry 81:918–929.
1059 Cheng Z, Zhou H, Sherva R, Farrer LA, Kranzler HR, Gelernter J (2018) Genome-wide
1060 Association Study Identifies a Regulatory Variant of RGMA Associated With Opioid
1061 Dependence in European Americans. Biol Psychiatry 84:762–770.
1062 Coffee and Caffeine Genetics Consortium et al. (2015) Genome-wide meta-analysis identifies six
1063 novel loci associated with habitual coffee consumption. Mol Psychiatry 20:647–656.
1064 Corces MR, Shcherbina A, Kundu S, Gloudemans MJ, Frésard L, Granja JM, Louie BH, Eulalio
1065 T, Shams S, Bagdatli ST, Mumbach MR, Liu B, Montine KS, Greenleaf WJ, Kundaje A,
1066 Montgomery SB, Chang HY, Montine TJ (2020) Single-cell epigenomic analyses
1067 implicate candidate causal variants at inherited risk loci for Alzheimer's and Parkinson's
1068 diseases. Nat Genet 52:1158–1168.
1069 Dashti HS et al. (2019) Genome-wide association study identifies genetic loci for self-reported
1070 habitual sleep duration supported by accelerometer-derived estimates. Nat Commun
1071 10:1100.
1072 Davis CA, Hitz BC, Sloan CA, Chan ET, Davidson JM, Gabdank I, Hilton JA, Jain K,
1073 Baymuradov UK, Narayanan AK, Onate KC, Graham K, Miyasato SR, Dreszer TR,
1074 Strattan JS, Jolanki O, Tanaka FY, Cherry JM (2018) The Encyclopedia of DNA
1075 elements (ENCODE): data portal update. Nucleic Acids Res 46:D794–D801.
1076 Dick DM (2016) The genetics of addiction: where do we go from here? J Stud Alcohol Drugs
1077 77:673–675.
1078 Eddie D, Greene MC, White WL, Kelly JF (2019) Medical burden of disease among individuals
1079 in recovery from alcohol and other drug problems in the united states: findings from the
1080 national recovery survey. J Addict Med 13:385–395.
1081 ENCODE Project Consortium (2012) An integrated encyclopedia of DNA elements in the
1082 human genome. Nature 489:57–74.
1083 Erzurumluoglu AM et al. (2019) Meta-analysis of up to 622,409 individuals identifies 40 novel
1084 smoking behaviour associated genetic loci. Mol Psychiatry.
1085 Farrell MR, Schoch H, Mahler SV (2018) Modeling cocaine relapse in rodents: Behavioral
1086 considerations and circuit mechanisms. Prog Neuropsychopharmacol Biol Psychiatry
1087 87:33–47.
1088 Fehr C, Yakushev I, Hohmann N, Buchholz H-G, Landvogt C, Deckers H, Eberhardt A, Kläger
1089 M, Smolka MN, Scheurich A, Dielentheis T, Schmidt LG, Rösch F, Bartenstein P,
1090 Gründer G, Schreckenberger M (2008) Association of low striatal dopamine d2 receptor
1091 availability with nicotine dependence similar to that seen with other drugs of abuse. Am J
1092 Psychiatry 165:507–514.
1093 Ferguson SM, Eskenazi D, Ishikawa M, Wanat MJ, Phillips PEM, Dong Y, Roth BL, Neumaier
1094 JF (2011) Transient neuronal inhibition reveals opposing roles of indirect and direct
1095 pathways in sensitization. Nat Neurosci 14:22–24.

1096 Finucane HK et al. (2015) Partitioning heritability by functional annotation using genome-wide
1097 association summary statistics. Nat Genet 47:1228–1235.
1098 Finucane HK et al. (2018) Heritability enrichment of specifically expressed genes identifies
1099 disease-relevant tissues and cell types. Nat Genet 50:621–629.
1100 Fullard JF, Hauberg ME, Bendl J, Egervari G, Cirnaru M-D, Reach SM, Motl J, Ehrlich ME,
1101 Hurd YL, Roussos P (2018) An atlas of chromatin accessibility in the adult human brain.
1102 Genome Res 28:1243–1252.
1103 GBD 2016 Alcohol and Drug Use Collaborators (2018) The global burden of disease attributable
1104 to alcohol and drug use in 195 countries and territories, 1990-2016: a systematic analysis
1105 for the Global Burden of Disease Study 2016. Lancet Psychiatry 5:987–1012.
1106 Ghandi M, Lee D, Mohammad-Noori M, Beer MA (2014) Enhanced regulatory sequence
1107 prediction using gapped k-mer features. PLoS Comput Biol 10:e1003711.
1108 Gjoneska E, Pfenning AR, Mathys H, Quon G, Kundaje A, Tsai L-H, Kellis M (2015)
1109 Conserved epigenomic signals in mice and humans reveal immune basis of Alzheimer's
1110 disease. Nature 518:365–369.
1111 Goldstein RZ, Volkow ND (2011) Dysfunction of the prefrontal cortex in addiction:
1112 neuroimaging findings and clinical implications. Nat Rev Neurosci 12:652–669.
1113 Grillner S, Robertson B (2016) The basal ganglia over 500 million years. Curr Biol 26:R1088–
1114 R1100.
1115 GTEx Consortium (2013) The Genotype-Tissue Expression (GTEx) project. Nat Genet 45:580–
1116 585.
1117 GTEx Consortium (2015) Human genomics. The Genotype-Tissue Expression (GTEx) pilot
1118 analysis: multitissue gene regulation in humans. Science 348:648–660.
1119 GTEx Consortium et al. (2017) Genetic effects on gene expression across human tissues. Nature
1120 550:204–213.
1121 Gupta S, Stamatoyannopoulos JA, Bailey TL, Noble WS (2007) Quantifying similarity between
1122 motifs. Genome Biol 8:R24.
1123 Hickey G, Paten B, Earl D, Zerbino D, Haussler D (2013) HAL: a hierarchical format for storing
1124 and analyzing multiple genome alignments. Bioinformatics 29:1341–1342.
1125 Hodge RD et al. (2019) Conserved cell types with divergent features in human versus mouse
1126 cortex. Nature 573:61–68.
1127 Hoffman JL, Faccidomo S, Kim M, Taylor SM, Agoglia AE, May AM, Smith EN, Wong LC,
1128 Hodge CW (2019) Alcohol Drinking Exacerbates Neural and Behavioral Pathology in the
1129 3xTg-AD Mouse Model of Alzheimer's Disease. BioRxiv.
1130 Howson JMM et al. (2017) Fifteen new risk loci for coronary artery disease highlight arterial-
1131 wall-specific mechanisms. Nat Genet 49:1113–1119.
1132 International Obsessive Compulsive Disorder Foundation Genetics Collaborative (IOCDF-GC)
1133 and OCD Collaborative Genetics Association Studies (OCGAS) (2018) Revealing the
1134 complex genetic architecture of obsessive-compulsive disorder using meta-analysis. Mol
1135 Psychiatry 23:1181–1188.
1136 Jensen KP (2016) A Review of Genome-Wide Association Studies of Stimulant and Opioid Use
1137 Disorders. Mol Neuropsychiatry 2:37–45.
1138 Ji X, Saha S, Kolpakova J, Guildford M, Tapper AR, Martin GE (2017) Dopamine Receptors
1139 Differentially Control Binge Alcohol Drinking-Mediated Synaptic Plasticity of the Core
1140 Nucleus Accumbens Direct and Indirect Pathways. J Neurosci 37:5463–5474.
1141 Jiang C, Wang X, Le Q, Liu P, Liu C, Wang Z, He G, Zheng P, Wang F, Ma L (2019) Morphine

1142 coordinates SST and PV interneurons in the prelimbic cortex to disinhibit pyramidal
1143 neurons and enhance reward. Mol Psychiatry.
1144 Johnston KJA, Adams MJ, Nicholl BI, Ward J, Strawbridge RJ, Ferguson A, McIntosh AM,
1145 Bailey MES, Smith DJ (2019) Genome-wide association study of multisite chronic pain
1146 in UK Biobank. PLoS Genet 15:e1008164.
1147 Karlsson Linnér R et al. (2019) Genome-wide association analyses of risk tolerance and risky
1148 behaviors in over 1 million individuals identify hundreds of loci and shared genetic
1149 influences. Nat Genet 51:245–257.
1150 Kelley DR, Reshef YA, Bileschi M, Belanger D, McLean CY, Snoek J (2018) Sequential
1151 regulatory activity prediction across chromosomes with convolutional neural networks.
1152 Genome Res 28:739–750.
1153 Kelley DR, Snoek J, Rinn JL (2016) Basset: learning the regulatory code of the accessible
1154 genome with deep convolutional neural networks. Genome Res 26:990–999.
1155 Kemp JP et al. (2017) Identification of 153 new loci associated with heel bone mineral density
1156 and functional involvement of GPC6 in osteoporosis. Nat Genet 49:1468–1475.
1157 Kendler KS, Prescott CA (1998a) Cannabis use, abuse, and dependence in a population-based
1158 sample of female twins. Am J Psychiatry 155:1016–1022.
1159 Kendler KS, Prescott CA (1998b) Cocaine use, abuse and dependence in a population-based
1160 sample of female twins. Br J Psychiatry 173:345–350.
1161 Khan A, Riudavets Puig R, Boddie P, Mathelier A (2020) BiasAway: command-line and web
1162 server to generate nucleotide composition-matched DNA background sequences.
1163 Available at: https://biasaway.uio.no [Accessed July 1, 2020].
1164 Kichaev G, Roytman M, Johnson R, Eskin E, Lindström S, Kraft P, Pasaniuc B (2017) Improved
1165 methods for multi-trait fine mapping of pleiotropic risk loci. Bioinformatics 33:248–255.
1166 Kim C, Kim S, Lee KY, Kim NH, Kang E-Y, Oh Y-W, Shin C (2019) Differences in bone
1167 density on chest CT according to smoking status in males without chronic obstructive
1168 lung disease. Sci Rep 9:10467.
1169 Koob GF, Volkow ND (2010) Neurocircuitry of addiction. Neuropsychopharmacology 35:217–
1170 238.
1171 Koob GF, Volkow ND (2016) Neurobiology of addiction: a neurocircuitry analysis. Lancet
1172 Psychiatry 3:760–773.
1173 Korthauer K, Kimes PK, Duvallet C, Reyes A, Subramanian A, Teng M, Shukla C, Alm EJ,
1174 Hicks SC (2019) A practical guide to methods controlling false discoveries in
1175 computational biology. Genome Biol 20:118.
1176 Krienen FM et al. (2019) Innovations in primate interneuron repertoire. BioRxiv.
1177 Lake BB, Chen S, Sos BC, Fan J, Kaeser GE, Yung YC, Duong TE, Gao D, Chun J, Kharchenko
1178 PV, Zhang K (2018) Integrative single-cell analysis of transcriptional and epigenetic
1179 states in the human adult brain. Nat Biotechnol 36:70–80.
1180 Landt SG et al. (2012) ChIP-seq guidelines and practices of the ENCODE and modENCODE
1181 consortia. Genome Res 22:1813–1831.
1182 Lansink CS, Goltstein PM, Lankelma JV, Pennartz CMA (2010) Fast-spiking interneurons of the
1183 rat ventral striatum: temporal coordination of activity with principal cells and
1184 responsiveness to reward. Eur J Neurosci 32:494–508.
1185 Lawler AJ, Brown AR, Bouchard RS, Toong N, Kim Y, Velraj N, Fox G, Kleyman M, Kang B,
1186 Gittis AH, Pfenning AR (2020) Cell Type-Specific Oxidative Stress Genomic Signatures
1187 in the Globus Pallidus of Dopamine-Depleted Mice. J Neurosci 40:9772–9783.

1188 Lee D (2016) LS-GKM: a new gkm-SVM for large-scale datasets. Bioinformatics 32:2196–
1189 2198.
1190 Lee IS, Leem AY, Lee SH, Rhee Y, Ha Y, Kim YS (2016) Relationship between pulmonary
1191 function and bone mineral density in the Korean National Health and Nutrition
1192 Examination Survey. Korean J Intern Med 31:899–909.
1193 Lee JH, Ribeiro EA, Kim J, Ko B, Kronman H, Jeong YH, Kim JK, Janak PH, Nestler EJ, Koo
1194 JW, Kim J-H (2020) Dopaminergic regulation of nucleus accumbens cholinergic
1195 interneurons demarcates susceptibility to cocaine addiction. Biol Psychiatry.
1196 Lee JJ et al. (2018) Gene discovery and polygenic prediction from a genome-wide association
1197 study of educational attainment in 1.1 million individuals. Nat Genet 50:1112–1121.
1198 Lefort S, Tomm C, Floyd Sarria JC, Petersen CCH (2009) The excitatory neuronal network of
1199 the C2 barrel column in mouse primary somatosensory cortex. Neuron 61:301–316.
1200 Liao Y, Smyth GK, Shi W (2014) featureCounts: an efficient general purpose program for
1201 assigning sequence reads to genomic features. Bioinformatics 30:923–930.
1202 Liu C, Wang M, Wei X, Wu L, Xu J, Dai X, Xia J, Cheng M, Yuan Y, Zhang P, Li J, Feng T,
1203 Chen A, Zhang W, Chen F, Shang Z, Zhang X, Peters BA, Liu L (2019a) An ATAC-seq
1204 atlas of chromatin accessibility in mouse tissues. Sci Data 6:65.
1205 Liu M et al. (2019b) Association studies of up to 1.2 million individuals yield new insights into
1206 the genetic etiology of tobacco and alcohol use. Nat Genet 51:237–244.
1207 Love MI, Huber W, Anders S (2014) Moderated estimation of fold change and dispersion for
1208 RNA-seq data with DESeq2. Genome Biol 15:550–550.
1209 Maurano MT et al. (2012) Systematic localization of common disease-associated variation in
1210 regulatory DNA. Science 337:1190–1195.
1211 Melé M et al. (2015) The human transcriptome across tissues and individuals. Science 348:660–
1212 665.
1213 Minnoye L, Taskiran II, Mauduit D, Fazio M, Van Aerschot L, Hulselmans G, Christiaens V,
1214 Makhzami S, Seltenhammer M, Karras P, Primot A, Cadieu E, van Rooijen E, Marine J-
1215 C, Egidy G, Ghanem GE, Zon L, Wouters J, Aerts S (2020) Cross-species analysis of
1216 enhancer logic using deep learning. Genome Res.
1217 Mo A, Mukamel EA, Davis FP, Luo C, Henry GL, Picard S, Urich MA, Nery JR, Sejnowski TJ,
1218 Lister R, Eddy SR, Ecker JR, Nathans J (2015) Epigenomic signatures of neuronal
1219 diversity in the mammalian brain. Neuron 86:1369–1384.
1220 Monaco G, van Dam S, Casal Novo Ribeiro JL, Larbi A, de Magalhães JP (2015) A comparison
1221 of human and mouse gene co-expression networks reveals conservation and divergence at
1222 the tissue, pathway and disease levels. BMC Evol Biol 15:259.
1223 Pasman JA et al. (2018) GWAS of lifetime cannabis use reveals new risk loci, genetic overlap
1224 with psychiatric traits, and a causal influence of schizophrenia. Nat Neurosci 21:1161–
1225 1170.
1226 Paten B, Earl D, Nguyen N, Diekhans M, Zerbino D, Haussler D (2011) Cactus: Algorithms for
1227 genome multiple sequence alignment. Genome Res 21:1512–1528.
1228 Pear VA, Ponicki WR, Gaidus A, Keyes KM, Martins SS, Fink DS, Rivera-Aguirre A,
1229 Gruenewald PJ, Cerdá M (2019) Urban-rural variation in the socioeconomic determinants
1230 of opioid overdose. Drug Alcohol Depend 195:66–73.
1231 Pelechano V, Steinmetz LM (2013) Gene regulation by antisense transcription. Nat Rev Genet
1232 14:880–893.
1233 Pullen E, Oser C (2014) Barriers to substance abuse treatment in rural and urban communities:

1234 counselor perspectives. Subst Use Misuse 49:891–901.
1235 Purcell S, Neale B, Todd-Brown K, Thomas L, Ferreira MAR, Bender D, Maller J, Sklar P, de
1236 Bakker PIW, Daly MJ, Sham PC (2007) PLINK: a tool set for whole-genome association
1237 and population-based linkage analyses. Am J Hum Genet 81:559–575.
1238 Ramamurthy E, Welch G, Cheng J, Yuan Y, Gunsalus L, Bennett DA, Tsai L-H, Pfenning A
1239 (2020) Cell type-specific histone acetylation profiling of Alzheimer's Disease subjects
1240 and integration with genetics. BioRxiv.
1241 Ramírez F, Bhardwaj V, Arrigoni L, Lam KC, Grüning BA, Villaveces J, Habermann B, Akhtar
1242 A, Manke T (2018) High-resolution TADs reveal DNA sequences underlying genome
1243 organization in flies. Nat Commun 9:189.
1244 Ramírez F, Ryan DP, Grüning B, Bhardwaj V, Kilpert F, Richter AS, Heyne S, Dündar F,
1245 Manke T (2016) deepTools2: a next generation web server for deep-sequencing data
1246 analysis. Nucleic Acids Res 44:W160-5.
1247 Ribeiro EA et al. (2018) Transcriptional and physiological adaptations in nucleus accumbens
1248 somatostatin interneurons that regulate behavioral responses to cocaine. Nat Commun
1249 9:3149.
1250 Roadmap Epigenomics Consortium et al. (2015) Integrative analysis of 111 reference human
1251 epigenomes. Nature 518:317–330.
1252 Saunders A, Macosko EZ, Wysoker A, Goldman M, Krienen FM, de Rivera H, Bien E, Baum M,
1253 Bortolin L, Wang S, Goeva A, Nemesh J, Kamitaki N, Brumbaugh S, Kulp D, McCarroll
1254 SA (2018) Molecular Diversity and Specializations among the Cells of the Adult Mouse
1255 Brain. Cell 174:1015–1030.e16.
1256 Scaplen KM, Kaun KR (2016) Reward from bugs to bipeds: a comparative approach to
1257 understanding how reward circuits function. J Neurogenet 30:133–148.
1258 Schall TA, Wright WJ, Dong Y (2020) Nucleus accumbens fast-spiking interneurons in
1259 motivational and addictive behaviors. Mol Psychiatry.
1260 Schizophrenia Working Group of the Psychiatric Genomics Consortium (2014) Biological
1261 insights from 108 schizophrenia-associated genetic loci. Nature 511:421–427.
1262 Seney M, Kim S-M, Wang J, Hildebrand M, Xue X, Glausier J, Zong W, Shelton M, Phan B,
1263 Srinivasan C, Pfenning A, Tseng G, Lewis D, Freyberg Z, Logan R (2020)
1264 Transcriptional alterations in opioid use disorder reveal an interplay between
1265 neuroinflammation and synaptic remodeling. BioRxiv.
1266 Shlyueva D, Stampfel G, Stark A (2014) Transcriptional enhancers: from properties to genome-
1267 wide predictions. Nat Rev Genet 15:272–286.
1268 Shrikumar A, Greenside P, Kundaje A (2017) Learning Important Features Through Propagating
1269 Activation Differences. arXiv.
1270 Shrikumar A, Tian K, Avsec Ž, Shcherbina A, Banerjee A, Sharmin M, Nair S, Kundaje A
1271 (2018) Technical Note on Transcription Factor Motif Discovery from Importance Scores
1272 (TF-MoDISco) version 0.5.6.5. arXiv.
1273 Smith LN (2018) A disciplined approach to neural network hyper-parameters: Part 1 -- learning
1274 rate, batch size, momentum, and weight decay. arXiv.
1275 Spitz F, Furlong EEM (2012) Transcription factors: from enhancer binding to developmental
1276 control. Nat Rev Genet 13:613–626.
1277 Štrumbelj E, Kononenko I (2014) Explaining prediction models and individual predictions with
1278 feature contributions. Knowl Inf Syst 41:647–665.
1279 Tak YG, Farnham PJ (2015) Making sense of GWAS: using epigenomics and genome

1280 engineering to understand the functional relevance of SNPs in non-coding regions of the
1281 human genome. Epigenetics Chromatin 8:57.
1282 Tepper JM, Koós T (2017) Gabaergic interneurons of the striatum. In: Handbook of basal
1283 ganglia structure and function, second edition, pp 157–178 Handbook of behavioral
1284 neuroscience. Elsevier.
1285 Thurman RE et al. (2012) The accessible chromatin landscape of the human genome. Nature
1286 489:75–82.
1287 Visscher PM, Wray NR, Zhang Q, Sklar P, McCarthy MI, Brown MA, Yang J (2017) 10 years
1288 of GWAS discovery: biology, function, and translation. Am J Hum Genet 101:5–22.
1289 Volkow ND, Chang L, Wang G-J, Fowler JS, Ding Y-S, Sedler M, Logan J, Franceschi D,
1290 Gatley J, Hitzemann R, Gifford A, Wong C, Pappas N (2003) Low level of brain
1291 dopamine d_2 receptors in methamphetamine abusers: association with metabolism in the
1292 orbitofrontal cortex. Focus (Madison) 1:150–157.
1293 Volkow ND, Morales M (2015) The brain on drugs: from reward to addiction. Cell 162:712–
1294 725.
1295 Volkow ND, Wang GJ, Fowler JS, Logan J, Gatley SJ, Hitzemann R, Chen AD, Dewey SL,
1296 Pappas N (1997) Decreased striatal dopaminergic responsiveness in detoxified cocaine-
1297 dependent subjects. Nature 386:830–833.
1298 Volkow ND, Wang GJ, Fowler JS, Logan J, Hitzemann R, Ding YS, Pappas N, Shea C, Piscani
1299 K (1996) Decreases in dopamine receptors but not in dopamine transporters in alcoholics.
1300 Alcohol Clin Exp Res 20:1594–1598.
1301 Volkow ND, Wang G-J, Tomasi D, Baler RD (2013) Unbalanced neuronal circuits in addiction.
1302 Curr Opin Neurobiol 23:639–648.
1303 Waaktaar T, Kan K-J, Torgersen S (2018) The genetic and environmental architecture of
1304 substance use development from early adolescence into young adulthood: a longitudinal
1305 twin study of comorbidity of alcohol, tobacco and illicit drug use. Addiction 113:740–
1306 748.
1307 Wang GJ, Volkow ND, Fowler JS, Logan J, Abumrad NN, Hitzemann RJ, Pappas NS, Pascani K
1308 (1997) Dopamine D2 receptor availability in opiate-dependent subjects before and after
1309 naloxone-precipitated withdrawal. Neuropsychopharmacology 16:174–182.
1310 Wang J, Huang D, Zhou Y, Yao H, Liu H, Zhai S, Wu C, Zheng Z, Zhao K, Wang Z, Yi X,
1311 Zhang S, Liu X, Liu Z, Chen K, Yu Y, Sham PC, Li MJ (2020) CAUSALdb: a database
1312 for disease/trait causal variants identified using summary statistics of genome-wide
1313 association studies. Nucleic Acids Res 48:D807–D816.
1314 Wang K, Li M, Hakonarson H (2010) ANNOVAR: functional annotation of genetic variants
1315 from high-throughput sequencing data. Nucleic Acids Res 38:e164.
1316 Ward LD, Kellis M (2016) HaploReg v4: systematic mining of putative causal variants, cell
1317 types, regulators and target genes for human complex traits and disease. Nucleic Acids
1318 Res 44:D877-81.
1319 Watanabe K, Taskesen E, van Bochoven A, Posthuma D (2017) Functional mapping and
1320 annotation of genetic associations with FUMA. Nat Commun 8:1826.
1321 Wilar G, Shinoda Y, Sasaoka T, Fukunaga K (2019) Crucial Role of Dopamine D2 Receptor
1322 Signaling in Nicotine-Induced Conditioned Place Preference. Mol Neurobiol 56:7911–
1323 7928.
1324 Wiltschko AB, Pettibone JR, Berke JD (2010) Opposite effects of stimulant and antipsychotic
1325 drugs on striatal fast-spiking interneurons. Neuropsychopharmacology 35:1261–1270.

1326 Worsley Hunt R, Mathelier A, Del Peso L, Wasserman WW (2014) Improving analysis of
1327 transcription factor binding sites within ChIP-Seq data based on topological motif
1328 enrichment. BMC Genomics 15:472.
1329 Xu Z, Liang Q, Song X, Zhang Z, Lindtner S, Li Z, Wen Y, Liu G, Guo T, Qi D, Wang M,
1330 Wang C, Li H, You Y, Wang X, Chen B, Feng H, Rubenstein JL, Yang Z (2018) SP8 and
1331 SP9 coordinately promote D2-type medium spiny neuron production by activating Six3
1332 expression. Development 145.
1333 Yue F et al. (2014) A comparative encyclopedia of DNA elements in the mouse genome. Nature
1334 515:355–364.
1335 Zeng X, Liu D, Zhao X, Chao L, Li Y, Li H, Li W, Gui L, Wu W (2019) Association of bone
1336 mineral density with lung function in a Chinese general population: the Xinxiang rural
1337 cohort study. BMC Pulm Med 19:239.
1338 Zhang X, Kaplow IM, Wirthlin M, Park TY, Pfenning AR (2020) HALPER facilitates the
1339 identification of regulatory element orthologs across species. Bioinformatics.
1340 Zhou J, Troyanskaya OG (2015) Predicting effects of non-coding variants with deep learning-
1341 based sequence model. Nat Methods 12:931–934.
1342 Zillikens MC et al. (2017) Large meta-analysis of genome-wide association studies identifies
1343 five loci for lean body mass. Nat Commun 8:80.
1344

1345 **Figure 1. Substance use and risky behavior GWAS risk variants enrich within reward**
1346 **region- and cell type-specific epigenomic profiles.**
1347 Partitioned LDSC regression (GWAS enrichment) finds enrichment of substance use and risky
1348 behavior traits in region-specific and cell type-specific open chromatin profiles of human
1349 postmortem brain. **(A)** Pie chart of ANNOVAR-annotated (Wang et al., 2010) SNP function of
1350 addiction-associated trait lead and off-lead SNPs in LD $R^2 > 0.8$. Dark colors indicate un-
1351 transcribed/non-coding annotations, light for transcribed/exonic annotations. SNP annotation
1352 labels are according to ANNOVAR using ENSEMBL build 85 gene annotations (Methods). **(B)**
1353 GWAS enrichment false-discovery rates in ATAC-seq of 14 postmortem human brain regions
1354 coupled with NeuN-labeled fluorescence activated nuclei sorting (Fullard et al., 2018). Brain
1355 regions are stratified by cortical and subcortical regions, with cortical regions ordered frontal to
1356 caudal. Sorted cell types within each brain region are denoted by shape (blue triangle for
1357 NeuN+/neuronal, red circle for NeuN-/glial). FDR-adjustment was performed across all
1358 enrichments on the Fullard *et al.* dataset for Figure 1B and Figure 3: **Cell type-specific**
1359 **convolutional neural network (CNN) models refine human NeuN+ enrichments for**
1360 **substance use genetic risk GWAS.**
1361 **(A) Schematic** to predict cell type-specific activity of NeuN+ ATAC-seq peaks enriched from
1362 brain regions assayed in Fullard *et al*. (Fullard et al., 2018) using **CNN** models trained on mouse
1363 cell-type specific ATAC-seq peaks. **CNN**-predicted OCRs are input into GWAS enrichment. **(B)**
1364 Partitioned LD score regression of addiction associated traits in Fullard *et al.* NeuN+ OCRs
1365 predicted to be cell type-specific by machine learning models of open chromatin. Cell types are
1366 colored by the source mouse cell type-specific OCRs from **Error! Reference source not**

1367 found.**A**. Original enrichments from Figure 1A are reproduced in black. **Larger, bolded points**
1368 **are significant for FDR < 0.05 (red dotted line)**.

1369

1370 **Figure 4: Convolutional Neural Network (CNN) models for predicting cell type-specific**
1371 **open chromatin predict activity of addiction GWAS SNPs**
1372 **(A) Cell type-activity predicted probability active by each set of CNN models of cell type**
1373 **activity for genome-wide significant SNPs and off-lead SNPs in LD R^2 > 0.8 with the lead**
1374 **SNPs.** Activity scores for SNPs are stratified by overlap with Fullard *et al.* (Fullard et al., 2018)
1375 cortical or striatal **NeuN+ (teal), NeuN- peaks (salmon), both (dark gray), or neither (light**
1376 **gray)**. Significance symbols denote Bonferroni-adjusted p-values from 2-tailed t-tests for N=18
1377 possible pairwise comparisons, N.S. not significant, * P < 0.05/N, ** P < 0.01/N, *** P <
1378 0.001/N. **(B)** Locus plot candidate SNP with predicted function SNP impact in **cortical**
1379 **excitatory and striatal D1, and D2 MSN** cell types. Genome tracks from top to bottom: **human**
1380 **(h)NeuN+ MACS2 ATAC-seq fold change signal of cortical and striatal brain** regions
1381 enriched in Figure 1A. SNP tracks **show lead SNPs aggregated across seven addiction-**
1382 **associated GWAS and the SNPs either in LD with the lead SNPs (Lead SNPs) or**
1383 **independently significant SNPs (LD/ Sig. SNPs). Each SNP is color by increasing red**
1384 **intensity by the degree of LD with a lead SNP. Prioritized candidate causal SNPs by**
1385 **predicted differential cell type activity and overlap with Fullard *et al.* NeuN+ OCRs are**
1386 **plot as (red for Tier A, yellow for Tier B, and teal for Tier C, Methods). Tier A SNP**
1387 **rs7604640 is predicted to have strong ΔSNP effect by CPU-D1 and NAc-D1 CNN models**
1388 **and the bars are colored by the % change in probability active. G**ene annotation tracks **plot**
1389 GENCODE **genes from the** GRCh38 **build**. eQTL link tracks of FDR-significant GTEX cis-

1390 eQTL from cortical and striatal brain **regions**, and orthologs **of mouse (m)** putative CREs
1391 mapped from **excitatory or striatal neuronal subtypes measured by** cSNAIL ATAC-seq. Cell
1392 type colors label cortical excitatory neurons (EXC; red), D1 medium spiny neurons (D1; blue),
1393 or D2 medium spiny neurons (D2; green). **(C) Representative importance scores of 50bp**
1394 **flanking either side of the SNP rs7604640 that measure relative contribution of that**
1395 **sequence being active in D1 MSNs. CNN importance score interpretations are shown for**
1396 **effect and non-effect alleles, and the difference in importance scores reveal the relatively**
1397 **more important DNA motif in the effect allele that matches consensus POU1F1 motif**
1398 **overlapping the rs7604640 SNP. The model interprets this POU1F1 motif and a nearby**
1399 **NRF1 motif as contributing to the effect allele having more activity in D1 MSNs.**

1400

1401 **Figure 5 Summary of LDSC GWAS enrichments in human and mouse-human orthologous**
1402 **bulk tissue and cell type open chromatin**
1403 **(A)** Schematic of human NeuN-labeled bulk tissue and occipital cortex cell types from **Figure 1**
1404 for which addiction-associated genetic variants were significantly enriched (FDR < 0.05) in
1405 OCRs. Brain regions are labelled by the cell type that enriched (NeuN+: blue box/shading;
1406 NeuN-: red box/shading) spatially along with the trait(s) for which OCRs were found
1407 significantly enriched with risk variants. Occipital cortex cell types from **Figure 1C** (same color
1408 scheme) are listed along with the trait(s) for which OCRs were found significantly enriched with
1409 risk variants. **(B)** Schematic of addiction-associated genetic variants that share enrichments from
1410 human brain regions and neuronal subtypes in both human and mouse-human orthologous open
1411 chromatin. Brain graphic adapted from Fullard *et al*.(Fullard et al., 2018)
1412

1413 **Supplemental Figure 1. Shared and unique genetic architecture of genetic risk variants of**
1414 **addiction-associated traits.**
1415 **(A)** LDSC genetic correlation (r_g) matrix of seven addiction-associated traits. FDR-significant
1416 correlations at shown in bold, non-significant in gray (FDR < 0.05). **(B)** Upset plot of **non-**
1417 **overlapping** genomic loci shared or unique to each addiction-associated trait. Genomic loci are
1418 **clustered and identified** by shared GWAS-significant SNPs and genomic region overlap.
1419
1420
1421 **Supplemental Figure** . **Brain regions reported to be significantly enriched (FDR <= 0.05)**
1422 **are plotted with bolded bars, and the significance threshold is represented by a dashed red**
1423 **line. (C) Barplot of GWAS enrichment false-discovery rates in single cell open chromatin**
1424 **profiles of cell clusters in isocortex, hippocampus, and striatum** (Corces et al., 2020)**. Cell**
1425 **types in brain regions that are significantly enriched (FDR <= 0.05) are plotted with bolded**
1426 **bars, and the significance threshold is represented by a dashed red line. (D) Barplot of**
1427 GWAS enrichment false-discovery rates in single cell THS-seq OCRs of major cell clusters in
1428 occipital cortex (Lake et al., 2018). Cell types in brain regions that are significantly enriched
1429 (FDR <= 0.05) are plotted with **bolded bars, and the significance threshold is represented by**
1430 **a dashed red line**. Traits assessed are age of smoking initiation (`AgeofInitiation`), average
1431 number of cigarettes per day for ever smokers (`CigarettesPerDay`), having ever regularly
1432 smoked (`SmokingInitiation`), current versus former smokers (SmokingCessation), number
1433 of alcoholic drinks per week (`DrinksPerWeek`) (Liu et al., 2019b), lifetime cannabis use
1434 (`Cannabis`) (Pasman et al., 2018), and risky behavior (`RiskyBehavior`) (Karlsson Linnér et
1435 al., 2019). OFC: orbitofrontal cortex, VLPFC: ventrolateral prefrontal cortex, DLPFC:

1436 dorsolateral prefrontal cortex, ACC: anterior cingulate cortex, INS: insula, STC: superior
1437 temporal gyrus, ITC: inferior temporal gyrus, PMC: primary motor cortex, PVC: primary visual
1438 cortex, AMY: amygdala, HIPP: hippocampus, MDT: mediodorsal thalamus, NAc: nucleus
1439 accumbens, PUT: putamen, Ast: astrocyte, End: endothelial, Ex: excitatory neuron, In: inhibitory
1440 neuron, Mic: microglia, Oli: oligodendrocyte, Opc: oligodendrocyte precursor.
1441
1442 **Figure 2: Cell type-specific enrichment of substance use traits are conserved in mouse-**
1443 **human orthologous open chromatin regions.**
1444 **(A)** Experimental design to map human orthologous regions from mouse ATAC-seq of bulk
1445 cortex (CTX), dorsal striatum (CPU), and nucleus accumbens (NAc) of cre-dependent Sun1-GFP
1446 Nuclear Anchored Independent Labeled (cSNAIL) nuclei of D1-cre, D2-cre, PV-cre, and SST-
1447 cre mice. cSNAIL ATAC-seq experiments report enriched (+) nuclei populations. **(B)** Partitioned
1448 LD score regression finds enrichment of substance use and risky behavior traits for brain region
1449 and cell type specific ATAC-seq open chromatin profiles of mouse brain. Replication of
1450 enrichment is shown using INTACT-enriched OCRs from Mo *et al* (Mo et al., 2015) of cortical
1451 excitatory (EXC+), vasoactive intestinal peptide interneuron (VIP+), and parvalbumin
1452 interneuron (PV+). Enrichments that are enriched at FDR < 0.05 are plotted with black outlines.
1453 FDR-adjusted p-value was performed across all mouse-human ortholog GWAS enrichment
1454 across Figure 2.
1455
1456 **Figure 3: Cell type-specific convolutional neural network (CNN) models refine human**
1457 **NeuN+ enrichments for substance use genetic risk GWAS.**

1458 **(A) Schematic** to predict cell type-specific activity of NeuN+ ATAC-seq peaks enriched from
1459 brain regions assayed in Fullard *et al*. (Fullard et al., 2018) using **CNN** models trained on mouse
1460 cell-type specific ATAC-seq peaks. **CNN**-predicted OCRs are input into GWAS enrichment. **(B)**
1461 Partitioned LD score regression of addiction associated traits in Fullard *et al.* NeuN+ OCRs
1462 predicted to be cell type-specific by machine learning models of open chromatin. Cell types are
1463 colored by the source mouse cell type-specific OCRs from **Error! Reference source not**
1464 **found.A**. Original enrichments from Figure 1A are reproduced in black. **Larger, bolded points**
1465 **are significant for FDR < 0.05 (red dotted line)**.

1466

1467 **Figure 4: Convolutional Neural Network (CNN) models for predicting cell type-specific**
1468 **open chromatin predict activity of addiction GWAS SNPs**
1469 **(A) Cell type-activity predicted probability active by each set of CNN models of cell type**
1470 **activity for genome-wide significant SNPs and off-lead SNPs in LD R^2 > 0.8 with the lead**
1471 **SNPs.** Activity scores for SNPs are stratified by overlap with Fullard *et al.* (Fullard et al., 2018)
1472 cortical or striatal **NeuN+ (teal), NeuN- peaks (salmon), both (dark gray), or neither (light**
1473 **gray)**. Significance symbols denote Bonferroni-adjusted p-values from 2-tailed t-tests for N=18
1474 possible pairwise comparisons, N.S. not significant, * P < 0.05/N, ** P < 0.01/N, *** P <
1475 0.001/N. **(B)** Locus plot candidate SNP with predicted function SNP impact in **cortical**
1476 **excitatory and striatal D1, and D2 MSN** cell types. Genome tracks from top to bottom: **human**
1477 **(h)NeuN+ MACS2 ATAC-seq fold change signal of cortical and striatal brain** regions
1478 enriched in Figure 1A. SNP tracks **show lead SNPs aggregated across seven addiction-**
1479 **associated GWAS and the SNPs either in LD with the lead SNPs (Lead SNPs) or**
1480 **independently significant SNPs (LD/ Sig. SNPs). Each SNP is color by increasing red**

1481 **intensity by the degree of LD with a lead SNP. Prioritized candidate causal SNPs by**
1482 **predicted differential cell type activity and overlap with Fullard *et al.* NeuN+ OCRs are**
1483 **plot as (red for Tier A, yellow for Tier B, and teal for Tier C, Methods). Tier A SNP**
1484 **rs7604640 is predicted to have strong ΔSNP effect by CPU-D1 and NAc-D1 CNN models**
1485 **and the bars are colored by the % change in probability active. G**ene annotation tracks **plot**
1486 GENCODE **genes from the** GRCh38 **build**. eQTL link tracks of FDR-significant GTEX cis-
1487 eQTL from cortical and striatal brain **regions**, and orthologs **of mouse (m)** putative CREs
1488 mapped from **excitatory or striatal neuronal subtypes measured by** cSNAIL ATAC-seq. Cell
1489 type colors label cortical excitatory neurons (EXC; red), D1 medium spiny neurons (D1; blue),
1490 or D2 medium spiny neurons (D2; green). **(C) Representative importance scores of 50bp**
1491 **flanking either side of the SNP rs7604640 that measure relative contribution of that**
1492 **sequence being active in D1 MSNs. CNN importance score interpretations are shown for**
1493 **effect and non-effect alleles, and the difference in importance scores reveal the relatively**
1494 **more important DNA motif in the effect allele that matches consensus POU1F1 motif**
1495 **overlapping the rs7604640 SNP. The model interprets this POU1F1 motif and a nearby**
1496 **NRF1 motif as contributing to the effect allele having more activity in D1 MSNs.**

1497

1498 **Figure 5 Summary of LDSC GWAS enrichments in human and mouse-human orthologous**
1499 **bulk tissue and cell type open chromatin**
1500 **(A)** Schematic of human NeuN-labeled bulk tissue and occipital cortex cell types from **Figure 1**
1501 for which addiction-associated genetic variants were significantly enriched (FDR < 0.05) in
1502 OCRs. Brain regions are labelled by the cell type that enriched (NeuN+: blue box/shading;
1503 NeuN-: red box/shading) spatially along with the trait(s) for which OCRs were found

1504 significantly enriched with risk variants. Occipital cortex cell types from **Figure 1C** (same color
1505 scheme) are listed along with the trait(s) for which OCRs were found significantly enriched with
1506 risk variants. **(B)** Schematic of addiction-associated genetic variants that share enrichments from
1507 human brain regions and neuronal subtypes in both human and mouse-human orthologous open
1508 chromatin. Brain graphic adapted from Fullard *et al*.(Fullard et al., 2018)
1509
1510 **Supplemental Figure 1. Shared and unique genetic architecture of genetic risk variants of**
1511 **addiction-associated traits.**
1512 **(A)** LDSC genetic correlation (r_g) matrix of seven addiction-associated traits. FDR-significant
1513 correlations at shown in bold, non-significant in gray (FDR < 0.05). **(B)** Upset plot of **non-**
1514 **overlapping** genomic loci shared or unique to each addiction-associated trait. Genomic loci are
1515 **clustered and identified** by shared GWAS-significant SNPs and genomic region overlap.
1516
1517
1518 **Supplemental Figure 2. Sensitivity of partitioned LDSC regression for cell type- and**
1519 **region-specific in the GWAS trait enrichment requires well-powered GWAS in relevant**
1520 **cell types.**
1521 GWAS enrichment plots with false-discovery rates in ATAC-seq of 14 postmortem human brain
1522 regions coupled with NeuN-labeled fluorescence activated nuclei sorting(Fullard et al., 2018).
1523 Regions are stratified by cortical and subcortical regions, with cortical regions ordered frontal to
1524 caudal. Sorted cell types within each brain region are denoted by shape (blue triangle for
1525 NeuN+/neuronal, red circle for NeuN-/glial). Cell types in brain regions that are enriched at FDR
1526 < 0.05 are plotted with bigger shapes and with black outlines. **(A)** GWAS enrichment of

1527 addiction- or substance use-associated traits: multi-site chronic pain (ChronicPain) (Johnston
1528 et al., 2019), cocaine dependence (CocaineDep) (Cabana-Domínguez et al., 2019) , opioid
1529 dependence (OpioidDep)(Cheng et al., 2018), diagnosis of obsessive-compulsive disorder
1530 (OCD) (International Obsessive Compulsive Disorder Foundation Genetics Collaborative
1531 (IOCDF-GC) and OCD Collaborative Genetics Association Studies (OCGAS), 2018), and cups
1532 of coffee drank per day (CoffeePerDay) (Coffee and Caffeine Genetics Consortium et al.,
1533 2015). The GWAS for OCD, opioid dependence, and cocaine dependence are reportedly
1534 underpowered to detect genetic liability for these traits (N_{case}< 5,000). **(B)** GWAS enrichment in
1535 well-powered brain-related traits show cell type- and region-specific enrichment: educational
1536 attainment (EduAttain) (Lee et al., 2018), schizophrenia risk (Schizophrenia) (Schizophrenia
1537 Working Group of the Psychiatric Genomics Consortium, 2014), habitual sleep duration
1538 (SleepDuration) (Dashti et al., 2019). **(C)** GWAS enrichment in non-brain associated traits
1539 do not show cell type- or region-specific enrichment: heel bone-mineral density (BMD) (Kemp et
1540 al., 2017), coronary artery disease (CAD) (Howson et al., 2017), and lean body mass (LBM)
1541 (Zillikens et al., 2017).

1542

1543 **Supplemental Figure 3. Cell type specificity of cSNAIL ATAC-seq in mouse cortex and**
1544 **striatum**

1545 (A) Principle component plots of chromatin accessibility counts from *cre*-dependent Sun1-GFP
1546 Nuclear Anchored Independent Labeled (cSNAIL) ATAC-seq from *cre*-driver lines (**Methods**).
1547 Major axes of variation separate cell types by tissue source (PC1) and cell type versus bulk
1548 ATAC-seq (PC2). (B) Normalized coverage track plots around marker genes demarcating cell
1549 type-specificity of cSNAIL ATAC-seq samples. (C) Density correlation plot of normalized

1550 chromatin accessibility log counts around the transcription start site (TSS) **correlated** with
1551 matched pseudo-bulk cell type log gene counts from Drop-seq of mouse cortex and
1552 striatum(Saunders et al., 2018). Drop-seq cell types meta-gene profiles report sum gene counts
1553 for cell clusters from frontal cortex and striatum. Pearson's and Spearman's correlation are
1554 denoted with R and ρ, respectively. (D) Pairwise correlation matrix of TSS chromatin
1555 accessibility log counts with Drop-seq pseudo-bulk log gene counts from cortical and striatal cell
1556 clusters.

1557
1558

1559 **Supplemental Figure 4. GWAS enrichment in addiction- and non-addiction-related traits**
1560 **using mapped mouse orthologs of tissue- and cell type-specific open chromatin regions.**
1561 GWAS enrichment plots with false-discovery rates in human orthologous regions mapped from
1562 mouse ATAC-seq of bulk cortex (CTX), dorsal striatum (CPU), and nucleus accumbens (**NAc**)
1563 or cre-dependent Sun1-GFP Nuclear Anchored Independent Labeled (cSNAIL) nuclei of D1-cre,
1564 D2-cre, and PV-cre mice. cSNAIL ATAC-seq experiments report both enriched (+) and de-
1565 enriched (-) nuclei populations. Enrichments that are enriched at FDR < 0.05 are plot with black
1566 outlines. Replication of enrichment is shown using INTACT-enriched OCRs from Mo *et al*(Mo
1567 et al., 2015) of cortical excitatory (EXC+), vasoactive intestinal peptide interneuron (VIP+), and
1568 parvalbumin interneuron (PV+). **(A)** GWAS enrichment of addiction- or substance use-
1569 associated traits: multi-site chronic pain (`ChronicPain`), cocaine dependence
1570 (`CocaineDep`), opioid dependence (`OpioidDep`), diagnosis of obsessive-compulsive disorder
1571 (`OCD`), and cups of coffee drank per day (`CoffeePerDay`). The GWAS for OCD, opioid
1572 dependence, and cocaine dependence are reportedly underpowered to detect genetic liability for
1573 these traits (N_{case}< 5,000). **(B)** GWAS enrichment in well-powered brain-related traits show cell

1574 type- and region-specific enrichment: educational attainment (`EduAttain`), schizophrenia risk
1575 (`Schizophrenia`), habitual sleep duration (`SleepDuration`). **(C)** GWAS enrichment in
1576 non-brain associated traits do not show cell type- or region-specific enrichment: heel bone-
1577 mineral density (`BMD`), coronary artery disease (`CAD`), and lean body mass (`LBM`). **(D)** Heatmap
1578 of LDSC regression coefficients of GWAS enrichment for all measured GWAS in non-brain
1579 OCRs from human or mouse-human mapped orthologs. Tissues for which OCRs are
1580 significantly enriched (FDR < 0.05) with GWAS variants are outlined with a bolded box.

1581

1582 **Supplemental Figure 5. Convolutional Neural Network (CNN) model performance and**
1583 **selection of candidate functional SNPs.**
1584 **(A)** Performance metrics for **convolutional neural network (CNN)** models **show high**
1585 **specificity on the test sets of positive peaks or 10x nucleotide-content matched negatives.**
1586 **Test set** performance metrics are reported for area under the precision-recall curve (auPRC)**, F1-**
1587 **score (using threshold = 0.5), and false positive rates across all possible thresholds**
1588 (**Methods**). Models were trained on IDR peaks of mouse cortical excitatory **(Ctx-EXC)** and D1
1589 and D2 medium spiny **neurons from caudoputamen (CPU) and the nucleus accumbens**
1590 **(NAc). (B) The models best discriminate the proportion of positives and negative sequences**
1591 **at a threshold of 0.5. Plots show the proportion of positives (blue) or negatives (red) that**
1592 **are called "positive" across CNN output thresholds from 0 to 1 averaged across folds for**
1593 **each set of CNN models. (C) Quantile-quantile plots of p-values of calibrated ΔSNP**
1594 **probability (Methods) from a normal distribution after centering by the mean and scaling**
1595 **by the standard deviation of delta SNP probabilities across all SNPs (n=14,790 SNPs) for**
1596 **each set of CNN models. A hexbin plot was used instead to better visualize over-plotting**

1597 **where every hexagon is color by the number of SNPs in that observed and expected p-**
1598 **value. The black dotted line denotes the equality line y = x. The number of significant SNPs**
1599 **at false discovery q-value < 0.05 at Tier A or B are reported for each cell type and tissue**
1600 **(Methods). (D) Schematic to select for predicted causal impact addiction-associated GWAS**
1601 **SNPs. The pipeline begins with SNPs across addiction-associated GWAS aggregated to 205**
1602 **non-overlapping GWAS loci across 14,790 SNPs after LD-expansion to include those in LD**
1603 **R^2 > 0.8. SNPs are further prioritized into three tiers. Tier C includes SNPs with only**
1604 **overlap with Fullard *et al.* NeuN+ ATAC-seq peaks, Tier B includes SNPs with only**
1605 **predicted significant differential allelic impact by on CNN-predicted CRE activity at q-**
1606 **value < 0.05, and Tier A include SNPs matching both criteria (Methods). (E) Outline of**
1607 **predicting differential CRE activity between alleles using calibrated CNN probabilities of**
1608 **CRE activity while controlling for false discovery using informative covariates (Methods).**
1609 **(F) Example motif matches from Supplemental Table 2 of TomTom known transcription**
1610 **factor consensus motifs and the learned important features in CNN models for cortical**
1611 **excitatory and striatal D1 and D2 MSNs.**

1612

1613 **Supplemental Figure 6. Locus plots of addiction-associated SNPs predicted to act in striatal**
1614 **and cortical cell types.**
1615 **Locus plot across four additional loci with Tier A SNPs with predicted function SNP**
1616 **impact in cortical excitatory and striatal D1 and D2 MSN cell types. Genome tracks from**
1617 **top to bottom: human (h)NeuN+ MACS2 ATAC-seq fold change signal of cortical and**
1618 **striatal brain regions enriched in Figure 1A. SNP tracks plot lead SNPs aggregated across**
1619 **seven addiction-associated GWAS, the SNPs in LD with the lead SNPs (Lead SNPs) or**

1620 **independently significant SNPs (LD/ Sig. SNPs). Each SNP is colored by red increasing in**
1621 **intensity by the degree of LD with a lead SNP. Prioritized candidate causal SNPs by**
1622 **predicted differential cell type activity and overlap with Fullard *et al.* NeuN+ OCRs are**
1623 **plot as (red for Tier A, yellow for Tier B, and teal for Tier C, Methods). Tier A SNP**
1624 **rs7604640 is predicted to have strong ΔSNP effect by CPU-D1 and NAc-D1 CNN models**
1625 **and the bars are colored by the % change in probability active. Gene annotation tracks**
1626 **plot GENCODE genes from the GRCh38 build. eQTL link tracks of FDR-significant**
1627 **GTEX cis-eQTL from cortical and striatal brain regions, and orthologs of mouse (m)**
1628 **putative CREs mapped from excitatory or striatal neuronal subtypes measured by cSNAIL**
1629 **ATAC-seq. NeuN+ ATAC-seq tracks and eQTL links are colored by source brain region as**
1630 **cortical (teal) or striatal (blue). Cell type colors label cortical excitatory neurons (EXC;**
1631 **red), D1 medium spiny neurons (D1; blue), or D2 medium spiny neurons (D2; green).**

1632 **Supplemental Table 1. Addiction-associated genetic variants annotated with cell type and**
1633 **brain region functional markers**
1634 **Addiction-associated genetic variants from the main seven GWAS (Figure 1) that were**
1635 **scored by CNN models along with computed raw CNN scores, predicted probability active,**
1636 **and ΔSNP probabilities, and tier of predicted candidate causal SNP. Each entry is recorded**
1637 **for a distinct SNP, predicted CNN model, and GWAS trait. Additional columns reporting**
1638 **are** annotated by FUMA (Watanabe et al., 2017) **and** CAUSALdb **(Wang et al., 2020). SNPs**
1639 **are annotated in this study to** overlap with **human** NeuN+ OCRs (Fullard et al., 2018). **A**
1640 **complete legend describing column headers is in the first sheet of the table.**
1641

1642 **Supplemental Table 2. TomTom matches with motifs learned by CNN models in each cell**
1643 **type and fold to contribute to a strong positive prediction. Learned important features**
1644 **were interpreted by DeepSHAP and clustered into unique seqlets by TF-Modisco**
1645 **(Methods).**
1646

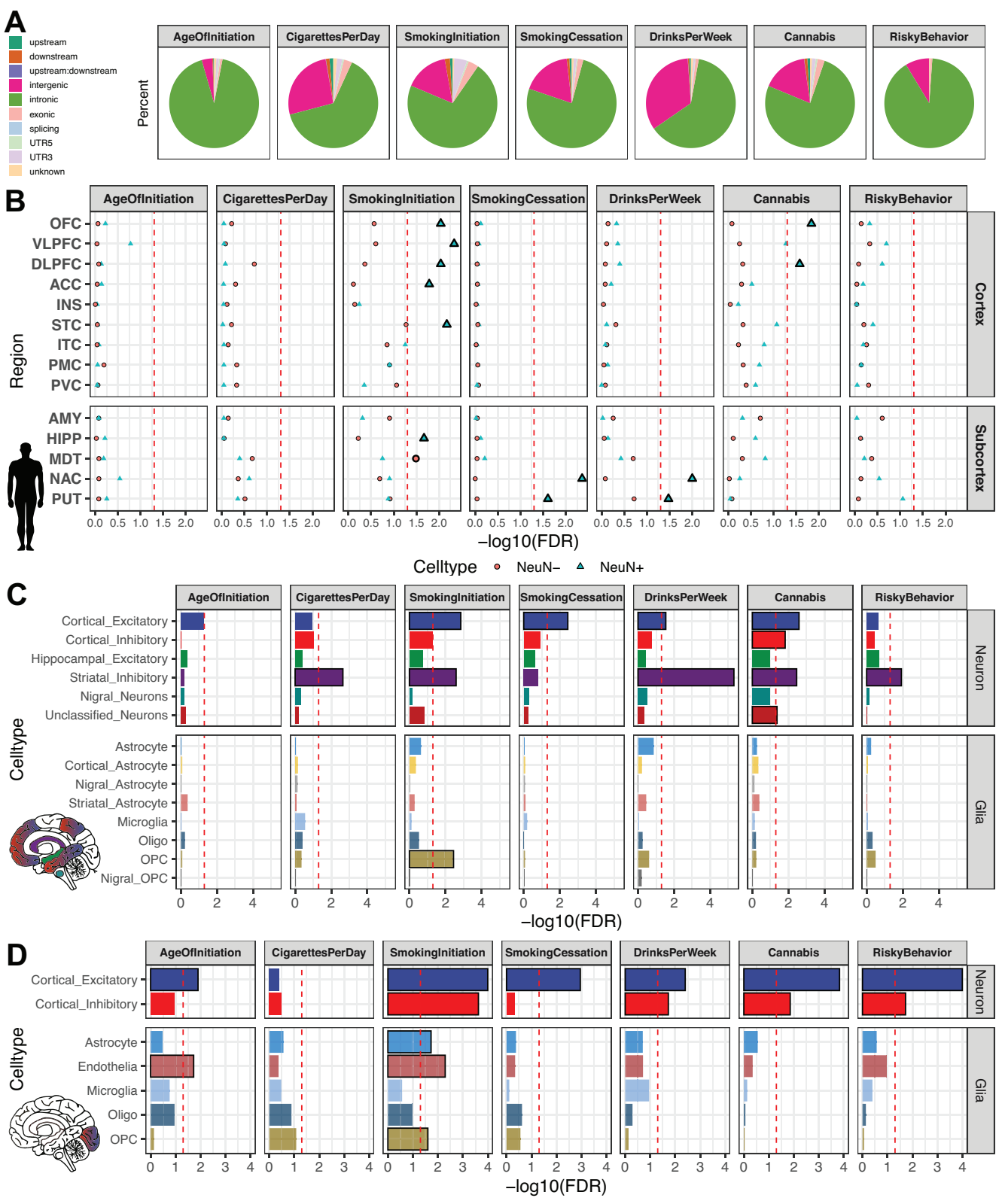
A
upstream
downstream
upstream:downstream
intergenic
intronic
exonic
splicing
UTR5
UTR3
unknown
Percent
AgeOfInitiation
CigarettesPerDay
SmokingInitiation
SmokingCessation
DrinksPerWeek
Cannabis
RiskyBehavior
B
Region
OFC
VLPFC
DLPFC
ACC
INS
STC
ITC
PMC
PVC
AMY
HIPP
MDT
NAC
PUT
Cortex
Subcortex
0.0 0.5 1.0 1.5 2.0
−log10(FDR)
Celltype
NeuN−
NeuN+
C
Celltype
Cortical_Excitatory
Cortical_Inhibitory
Hippocampal_Excitatory
Striatal_Inhibitory
Nigral_Neurons
Unclassified_Neurons
Astrocyte
Cortical_Astrocyte
Nigral_Astrocyte
Striatal_Astrocyte
Microglia
Oligo
OPC
Nigral_OPC
Neuron
Glia
0 2 4
−log10(FDR)
D
Cortical_Excitatory
Cortical_Inhibitory
Astrocyte
Endothelia
Microglia
Oligo
OPC
Neuron
Glia
0 1 2 3 4
−log10(FDR)

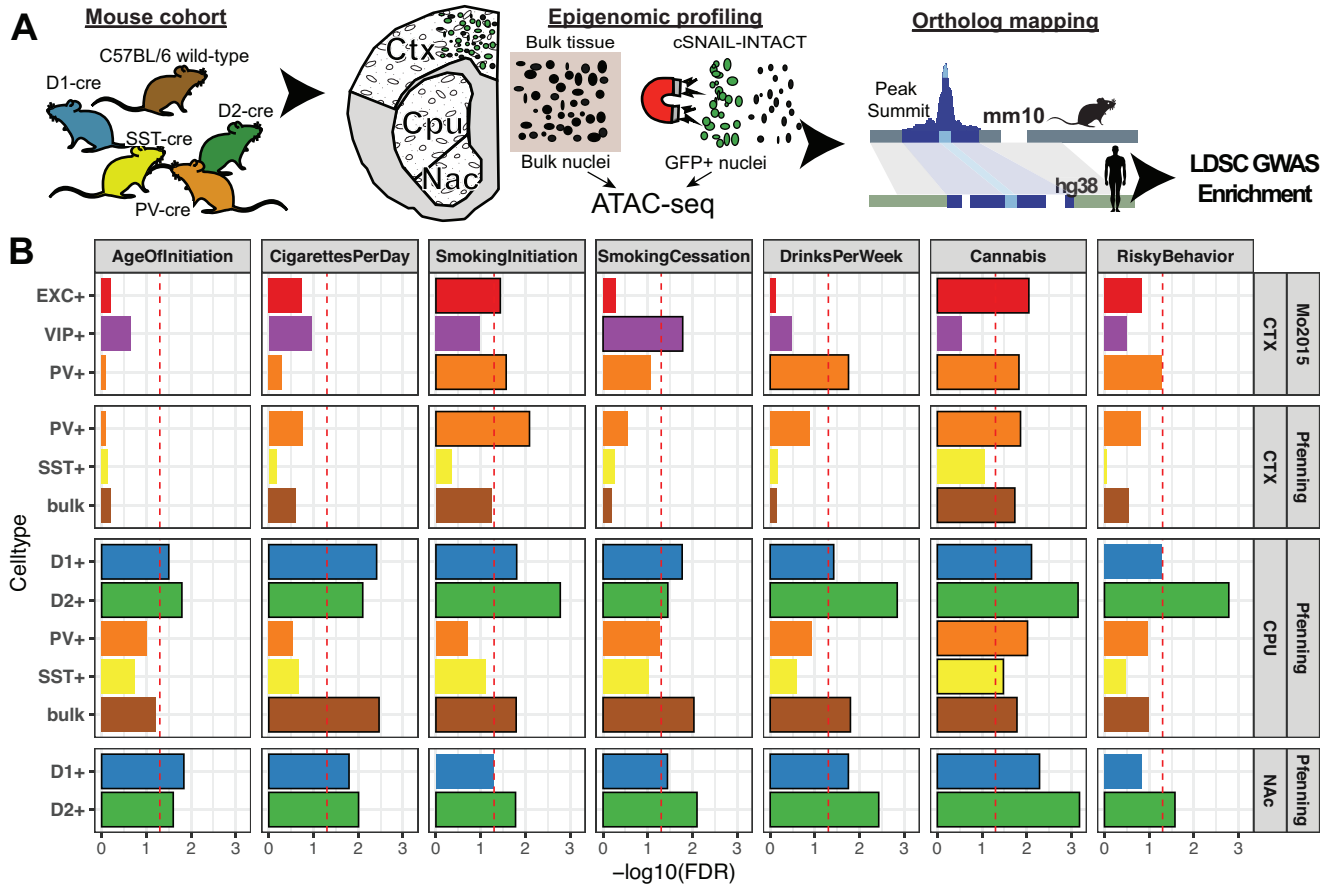
A
Mouse cohort
C57BL/6 wild-type
D1-cre
D2-cre
SST-cre
PV-cre
Ctx
Cpu
Nac
Epigenomic profiling
Bulk tissue
cSNAIL-INTACT
Bulk nuclei
GFP+ nuclei
ATAC-seq
Ortholog mapping
Peak Summit
mm10
hg38
LDSC GWAS Enrichment
B
AgeOfInitiation
CigarettesPerDay
SmokingInitiation
SmokingCessation
DrinksPerWeek
Cannabis
RiskyBehavior
Celltype
EXC+
VIP+
PV+
SST+
bulk
D1+
D2+
CTX
CPU
NAc
Mo2015
Pfenning
0
1
2
3
−log10(FDR)

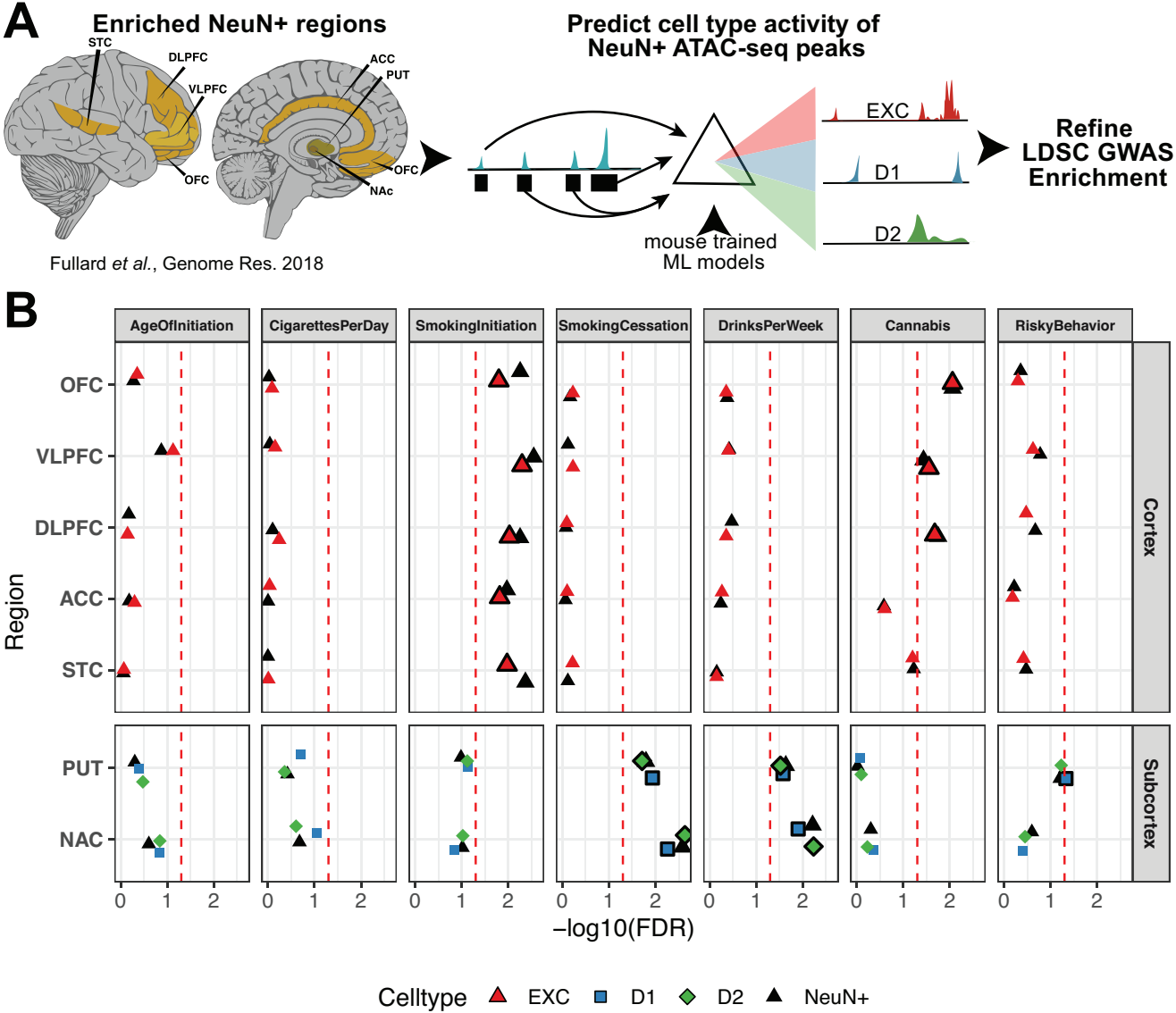
A
Enriched NeuN+ regions
STC
DLPFC
VLPFC
OFC
ACC
PUT
OFC
NAc
Fullard et al., Genome Res. 2018
Predict cell type activity of NeuN+ ATAC-seq peaks
mouse trained ML models
EXC
D1
D2
Refine LDSC GWAS Enrichment
B
AgeOfInitiation
CigarettesPerDay
SmokingInitiation
SmokingCessation
DrinksPerWeek
Cannabis
RiskyBehavior
Region
OFC
VLPFC
DLPFC
ACC
STC
PUT
NAC
Cortex
Subcortex
0
1
2
−log10(FDR)
Celltype
EXC
D1
D2
NeuN+

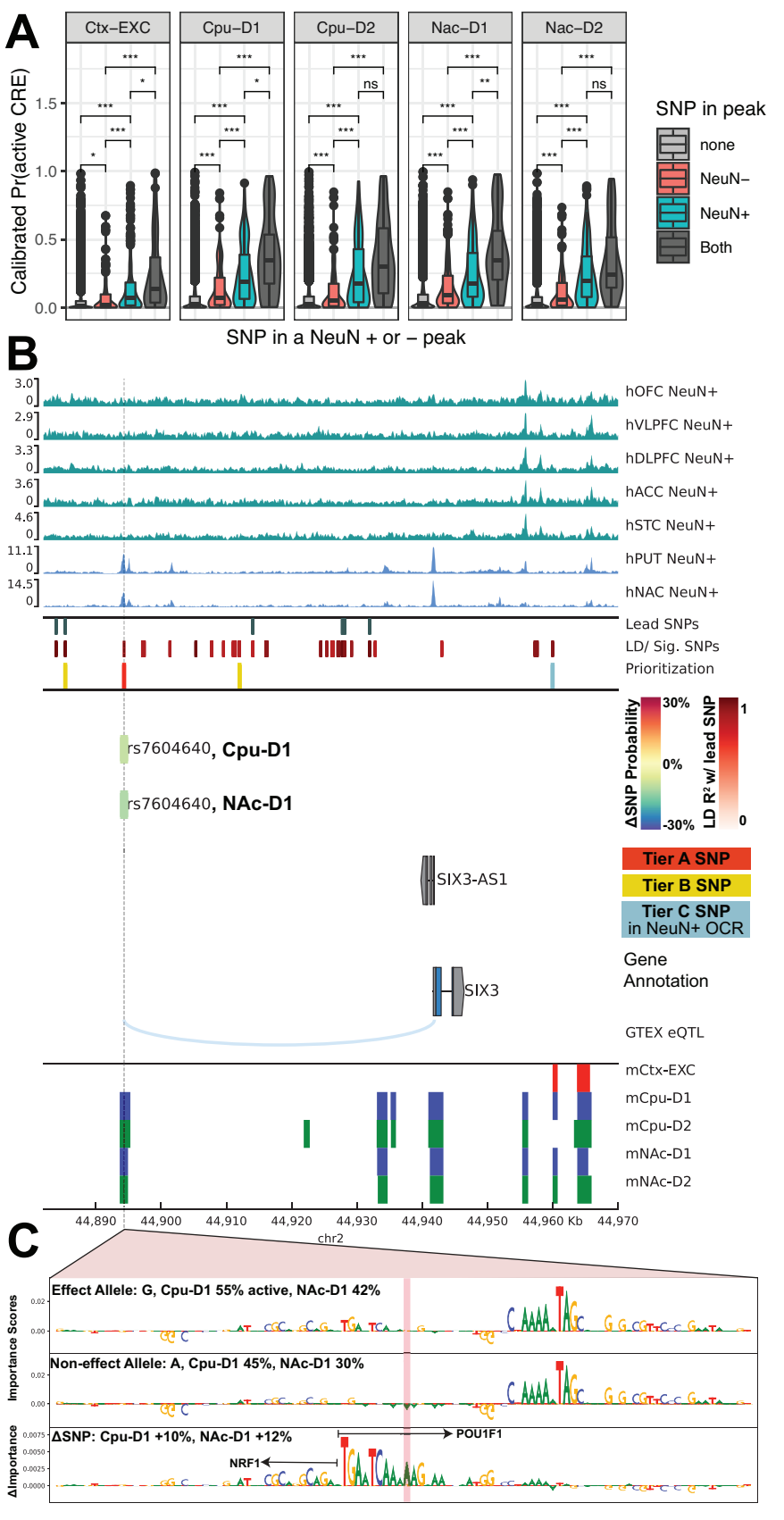
A
Ctx–EXC
Cpu–D1
Cpu–D2
Nac–D1
Nac–D2
Calibrated Pr(active CRE)
SNP in a NeuN + or – peak
SNP in peak
none
NeuN–
NeuN+
Both
B
hOFC NeuN+
hVLPFC NeuN+
hDLPFC NeuN+
hACC NeuN+
hSTC NeuN+
hPUT NeuN+
hNAC NeuN+
Lead SNPs
LD/ Sig. SNPs
Prioritization
ΔSNP Probability
LD R² w/ lead SNP
rs7604640, Cpu-D1
rs7604640, NAc-D1
SIX3-AS1
SIX3
Tier A SNP
Tier B SNP
Tier C SNP in NeuN+ OCR
Gene Annotation
GTEX eQTL
mCtx-EXC
mCpu-D1
mCpu-D2
mNAc-D1
mNAc-D2
chr2
C
Effect Allele: G, Cpu-D1 55% active, NAc-D1 42%
Non-effect Allele: A, Cpu-D1 45%, NAc-D1 30%
ΔSNP: Cpu-D1 +10%, NAc-D1 +12%
POU1F1
NRF1
Importance Scores
ΔImportance

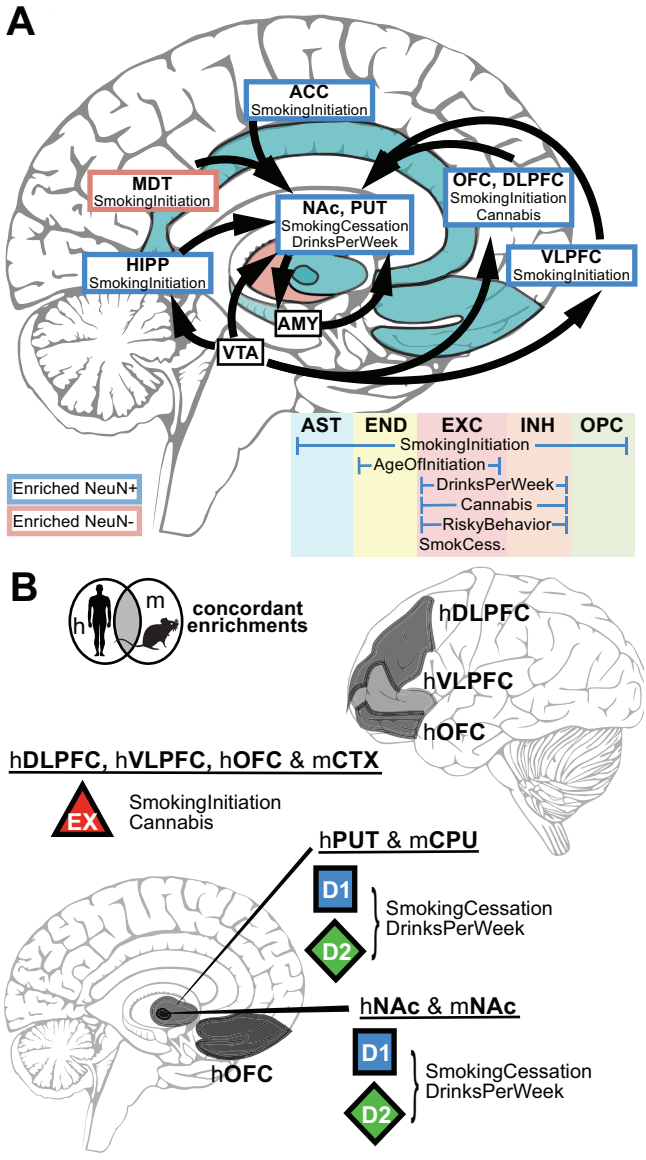
A
ACC
SmokingInitiation
MDT
SmokingInitiation
NAc, PUT
SmokingCessation
DrinksPerWeek
OFC, DLPFC
SmokingInitiation
Cannabis
HIPP
SmokingInitiation
VLPFC
SmokingInitiation
AMY
VTA
AST
END
EXC
INH
OPC
SmokingInitiation
AgeOfInitiation
DrinksPerWeek
Cannabis
RiskyBehavior
SmokCess.
Enriched NeuN+
Enriched NeuN-
B
h
m
concordant enrichments
hDLPFC
hVLPFC
hOFC
hDLPFC, hVLPFC, hOFC & mCTX
EX
SmokingInitiation
Cannabis
hPUT & mCPU
D1
D2
SmokingCessation
DrinksPerWeek
hNAc & mNAc
D1
D2
SmokingCessation
DrinksPerWeek
hOFC

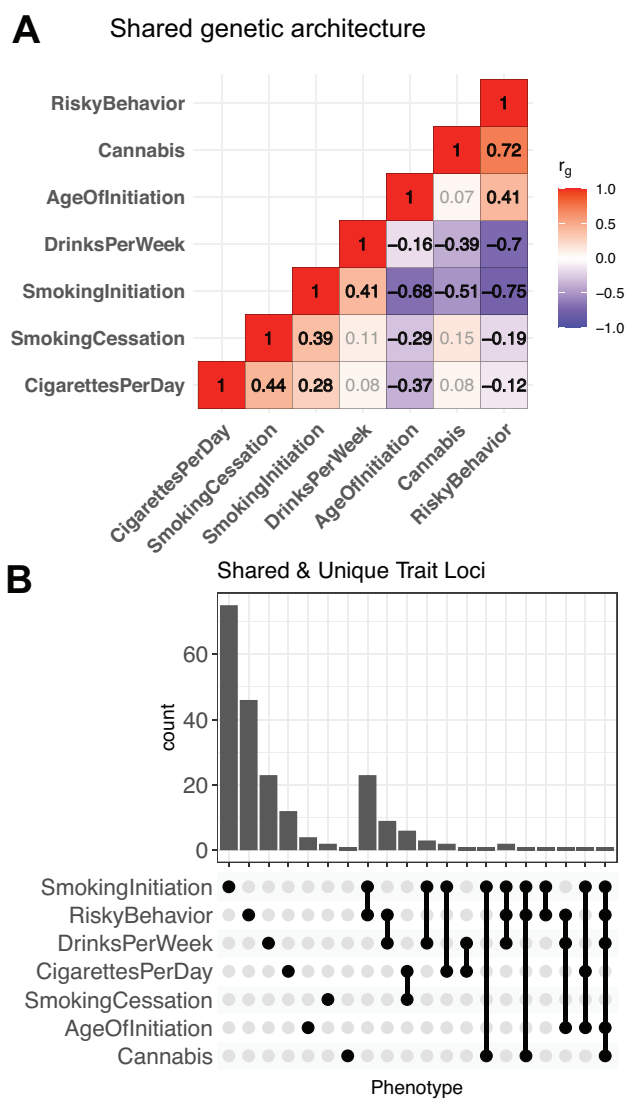
A
Shared genetic architecture
RiskyBehavior
Cannabis
AgeOfInitiation
DrinksPerWeek
SmokingInitiation
SmokingCessation
CigarettesPerDay
1
1 0.72
1 0.07 0.41
1 −0.16 −0.39 −0.7
1 0.41 −0.68 −0.51 −0.75
1 0.39 0.11 −0.29 0.15 −0.19
1 0.44 0.28 0.08 −0.37 0.08 −0.12
CigarettesPerDay
SmokingCessation
SmokingInitiation
DrinksPerWeek
AgeOfInitiation
Cannabis
RiskyBehavior
r_g
1.0
0.5
0.0
−0.5
−1.0
B
Shared & Unique Trait Loci
count
0
20
40
60
SmokingInitiation
RiskyBehavior
DrinksPerWeek
CigarettesPerDay
SmokingCessation
AgeOfInitiation
Cannabis
Phenotype

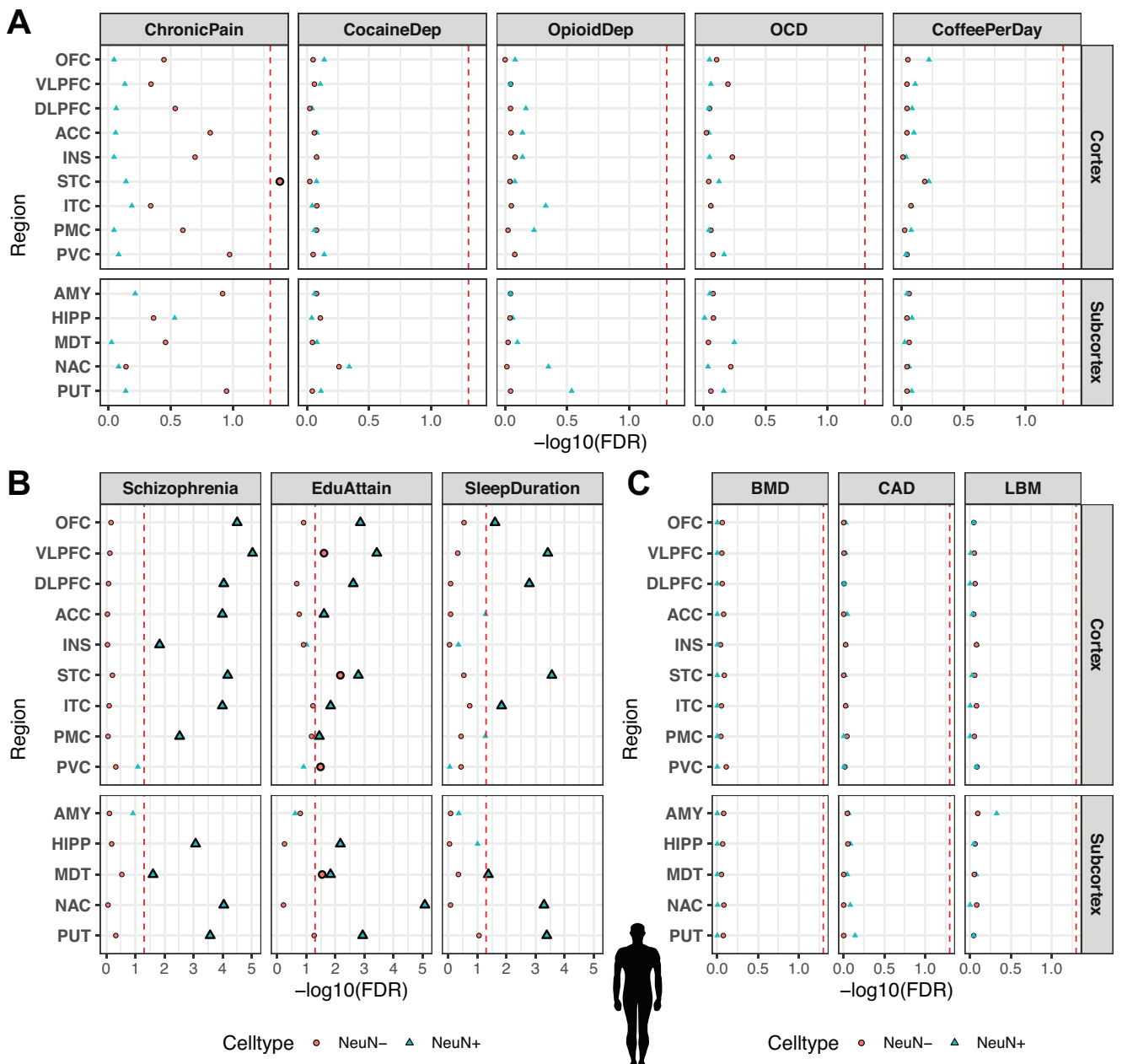
A
ChronicPain
CocaineDep
OpioidDep
OCD
CoffeePerDay
Cortex
Subcortex
Region
OFC
VLPFC
DLPFC
ACC
INS
STC
ITC
PMC
PVC
AMY
HIPP
MDT
NAC
PUT
0.0
0.5
1.0
−log10(FDR)
B
Schizophrenia
EduAttain
SleepDuration
0
1
2
3
4
5
C
BMD
CAD
LBM
Celltype
NeuN−
NeuN+

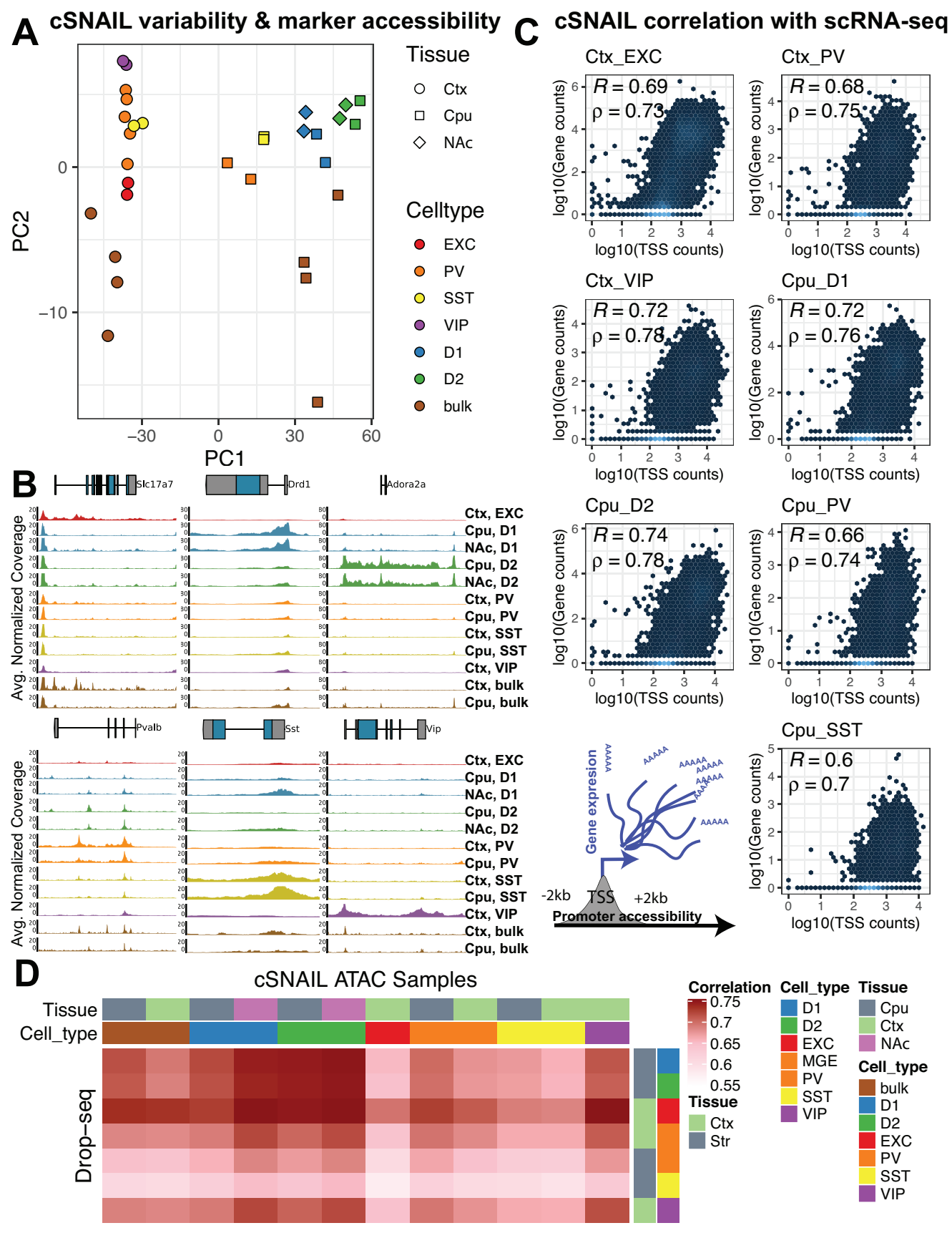
A
cSNAIL variability & marker accessibility
PC2
PC1
Tissue
Ctx
Cpu
NAc
Celltype
EXC
PV
SST
VIP
D1
D2
bulk
B
Slc17a7
Drd1
Adora2a
Avg. Normalized Coverage
Ctx, EXC
Cpu, D1
NAc, D1
Cpu, D2
NAc, D2
Ctx, PV
Cpu, PV
Ctx, SST
Cpu, SST
Ctx, VIP
Ctx, bulk
Cpu, bulk
Pvalb
Sst
Vip
C
cSNAIL correlation with scRNA-seq
Ctx_EXC
R = 0.69
ρ = 0.73
Ctx_PV
R = 0.68
ρ = 0.75
Ctx_VIP
R = 0.72
ρ = 0.78
Cpu_D1
R = 0.72
ρ = 0.76
Cpu_D2
R = 0.74
ρ = 0.78
Cpu_PV
R = 0.66
ρ = 0.74
Cpu_SST
R = 0.6
ρ = 0.7
log10(Gene counts)
log10(TSS counts)
Gene expression
-2kb
TSS
+2kb
Promoter accessibility
D
cSNAIL ATAC Samples
Tissue
Cell_type
Drop−seq
Correlation
Tissue
Ctx
Str
Cell_type
D1
D2
EXC
MGE
PV
SST
VIP
Tissue
Cpu
Ctx
NAc
Cell_type
bulk
D1
D2
EXC
PV
SST
VIP

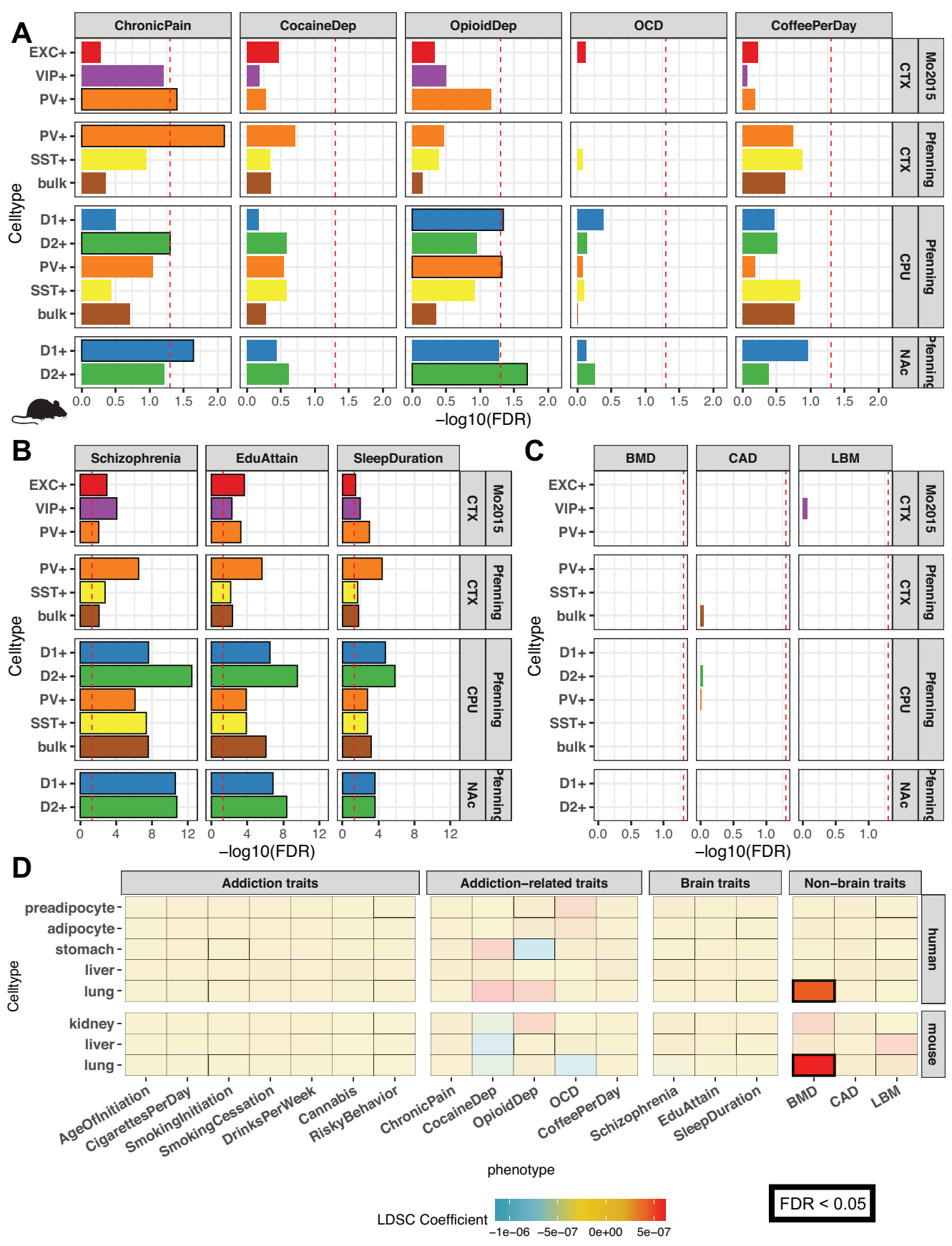
A
ChronicPain
CocaineDep
OpioidDep
OCD
CoffeePerDay
Celltype
EXC+
VIP+
PV+
SST+
bulk
D1+
D2+
CTX
CPU
NAc
Mo2015
Pfenning
–log10(FDR)
B
Schizophrenia
EduAttain
SleepDuration
C
BMD
CAD
LBM
D
Addiction traits
Addiction–related traits
Brain traits
Non–brain traits
preadipocyte
adipocyte
stomach
liver
lung
kidney
human
mouse
AgeOfInitiation
CigarettesPerDay
SmokingInitiation
SmokingCessation
DrinksPerWeek
Cannabis
RiskyBehavior
phenotype
LDSC Coefficient
–1e–06
–5e–07
0e+00
5e–07
FDR < 0.05

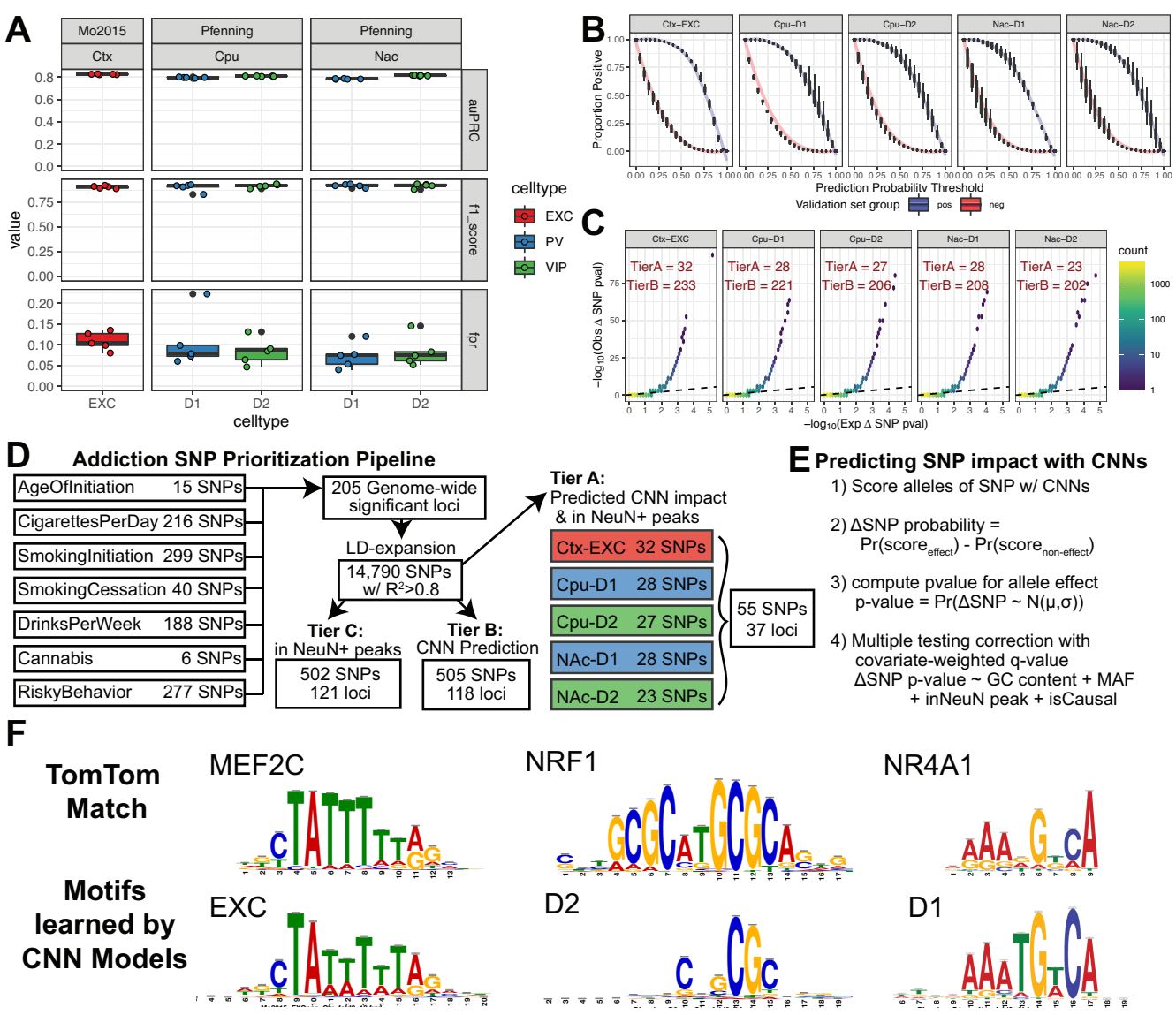
A
Mo2015
Pfenning
Pfenning
Ctx
Cpu
Nac
auPRC
f1_score
fpr
value
EXC
D1
D2
D1
D2
celltype
celltype
EXC
PV
VIP
B
Ctx−EXC
Cpu−D1
Cpu−D2
Nac−D1
Nac−D2
Proportion Positive
Prediction Probability Threshold
Validation set group
pos
neg
C
Ctx−EXC
Cpu−D1
Cpu−D2
Nac−D1
Nac−D2
TierA = 32
TierB = 233
TierA = 28
TierB = 221
TierA = 27
TierB = 206
TierA = 28
TierB = 208
TierA = 23
TierB = 202
count
−log10(Obs Δ SNP pval)
−log10(Exp Δ SNP pval)
D
Addiction SNP Prioritization Pipeline
AgeOfInitiation 15 SNPs
CigarettesPerDay 216 SNPs
SmokingInitiation 299 SNPs
SmokingCessation 40 SNPs
DrinksPerWeek 188 SNPs
Cannabis 6 SNPs
RiskyBehavior 277 SNPs
205 Genome-wide significant loci
LD-expansion
14,790 SNPs w/ R²>0.8
Tier C: in NeuN+ peaks
502 SNPs 121 loci
Tier B: CNN Prediction
505 SNPs 118 loci
Tier A: Predicted CNN impact & in NeuN+ peaks
Ctx-EXC 32 SNPs
Cpu-D1 28 SNPs
Cpu-D2 27 SNPs
NAc-D1 28 SNPs
NAc-D2 23 SNPs
55 SNPs 37 loci
E
Predicting SNP impact with CNNs
1) Score alleles of SNP w/ CNNs
2) ΔSNP probability = Pr(score_effect) - Pr(score_non-effect)
3) compute pvalue for allele effect p-value = Pr(ΔSNP ~ N(μ,σ))
4) Multiple testing correction with covariate-weighted q-value ΔSNP p-value ~ GC content + MAF + inNeuN peak + isCausal
F
TomTom Match
MEF2C
NRF1
NR4A1
Motifs learned by CNN Models
EXC
D2
D1

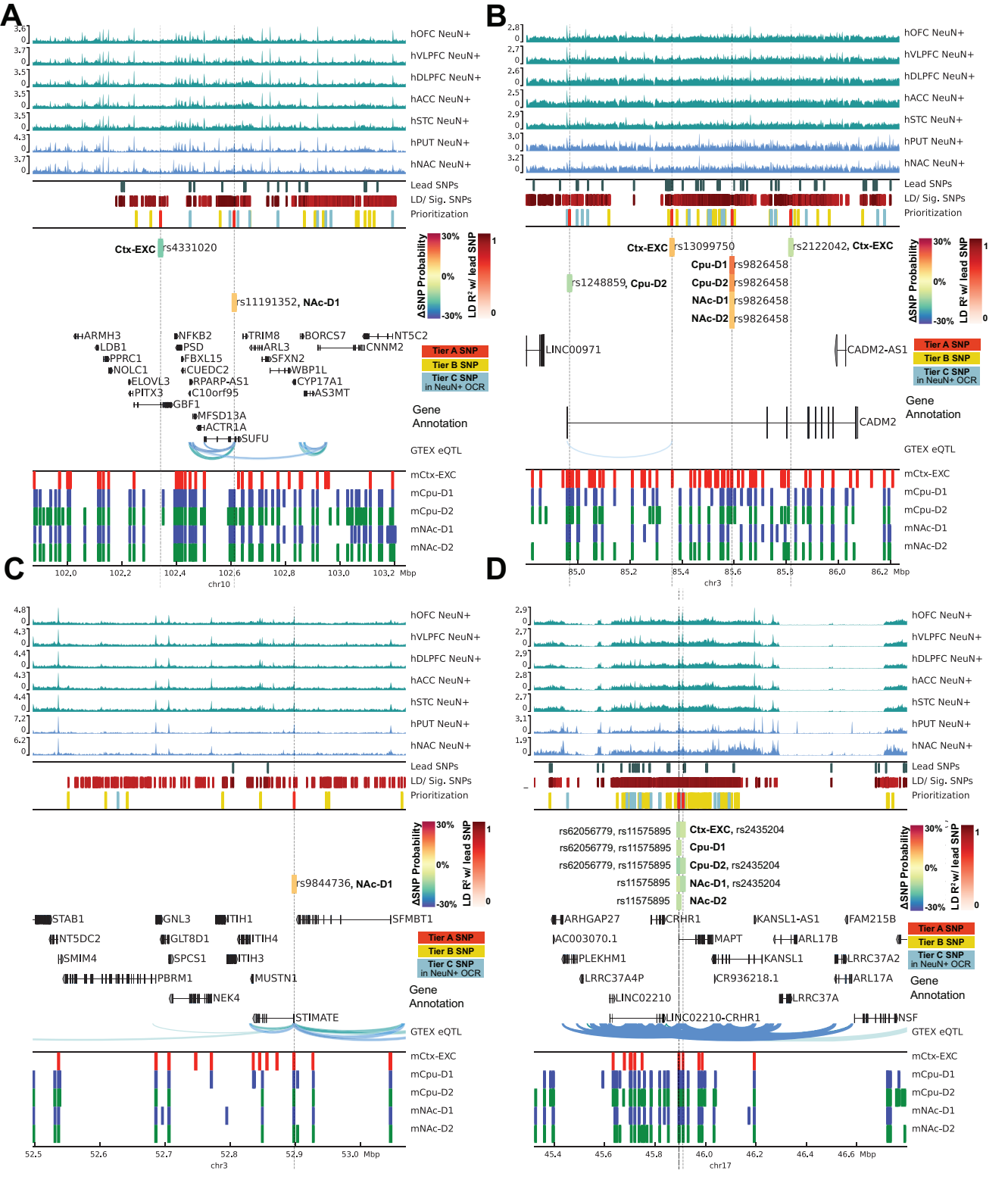
A
B
C
D
hOFC NeuN+
hVLPFC NeuN+
hDLPFC NeuN+
hACC NeuN+
hSTC NeuN+
hPUT NeuN+
hNAC NeuN+
Lead SNPs
LD/ Sig. SNPs
Prioritization
ΔSNP Probability
30%
0%
-30%
LD R² w/ lead SNP
Ctx-EXC rs4331020
rs11191352, NAc-D1
ARMH3
LDB1
PPRC1
NOLC1
ELOVL3
PITX3
GBF1
NFKB2
PSD
FBXL15
CUEDC2
RPARP-AS1
C10orf95
MFSD13A
ACTR1A
SUFU
TRIM8
ARL3
SFXN2
WBP1L
CYP17A1
AS3MT
BORCS7
CNNM2
NT5C2
Tier A SNP
Tier B SNP
Tier C SNP in NeuN+ OCR
Gene Annotation
GTEX eQTL
mCtx-EXC
mCpu-D1
mCpu-D2
mNAc-D1
mNAc-D2
102.0
102.2
102.4
102.6
102.8
103.0
103.2 Mbp
chr10
Ctx-EXC rs13099750
rs2122042, Ctx-EXC
Cpu-D1 rs9826458
Cpu-D2 rs9826458
NAc-D1 rs9826458
NAc-D2 rs9826458
rs1248859, Cpu-D2
LINC00971
CADM2-AS1
CADM2
85.0
85.2
85.4
85.6
85.8
86.0
86.2 Mbp
chr3
rs9844736, NAc-D1
STAB1
NT5DC2
SMIM4
GNL3
GLT8D1
SPCS1
PBRM1
NEK4
ITIH1
ITIH4
ITIH3
MUSTN1
SFMBT1
STIMATE
52.5
52.6
52.7
52.8
52.9
53.0 Mbp
chr3
rs62056779, rs11575895
Ctx-EXC, rs2435204
Cpu-D1
Cpu-D2, rs2435204
NAc-D1, rs2435204
NAc-D2
ARHGAP27
AC003070.1
PLEKHM1
LRRC37A4P
LINC02210
CRHR1
MAPT
KANSL1
CR936218.1
LINC02210-CRHR1
KANSL1-AS1
ARL17B
LRRC37A
FAM215B
LRRC37A2
ARL17A
NSF
45.4
45.6
45.8
46.0
46.2
46.4
46.6 Mbp
chr17